THE ISM PROPERTIES AND GAS KINEMATICS OF A REDSHIFT 3 MASSIVE DUSTY STAR-FORMING GALAXY

T. K. DAISY LEUNG[1,2], DOMINIK A. RIECHERS[1], ANDREW J. BAKER[3], DAVE L. CLEMENTS[4], ASANTHA COORAY[5], CHRISTOPHER C. HAYWARD[2], R. J. IVISON[6,7], ROBERTO NERI[8], ALAIN OMONT[9], ISMAEL PÉREZ-FOURNON[10,11], DOUGLAS SCOTT[12], AND JULIE L. WARDLOW[13,14]

Accepted to the ApJ

ABSTRACT

We present CO ($J = 1 \rightarrow 0$; $3 \rightarrow 2$; $5 \rightarrow 4$; $10 \rightarrow 9$) and 1.2-kpc resolution [CII] line observations of the dusty star-forming galaxy (SFG) HXMM05 — carried out with the Karl G. Jansky Very Large Array, the Combined Array for Research in Millimeter-wave Astronomy, the Plateau de Bure Interferometer, and the Atacama Large Millimeter/submillimeter Array, measuring an unambiguous redshift of $z = 2.9850 \pm 0.0009$. We find that HXMM05 is a hyper-luminous infrared galaxy ($L_{IR} = (4 \pm 1) \times 10^{13} L_\odot$) with a total molecular gas mass of $(2.1 \pm 0.7) \times 10^{11} (\alpha_{CO}/0.8) M_\odot$. The CO ($J = 1 \rightarrow 0$) and [CII] emission are extended over ~ 9 kpc in diameter, and the CO line FWHM exceeds 1100 km s^{-1}. The [CII] emission shows a monotonic velocity gradient consistent with a disk, with a maximum rotation velocity of $v_c = 616 \pm 100$ km s^{-1} and a dynamical mass of $(7.7 \pm 3.1) \times 10^{11} M_\odot$. We find a star formation rate (SFR) of $2900^{+750}_{-595} M_\odot$ yr^{-1}. HXMM05 is thus among the most intensely star-forming galaxies known at high redshift. Photo-dissociation region modeling suggests physical conditions similar to nearby SFGs, showing extended star formation, which is consistent with our finding that the gas and dust emission are co-spatial. Its molecular gas excitation resembles the local major merger Arp 220. The broad CO and [CII] lines and a pair of compact dust nuclei suggest the presence of a late-stage major merger at the center of the extended disk, again reminiscent of Arp 220. The observed gas kinematics and conditions together with the presence of a companion and the pair of nuclei suggest that HXMM05 is experiencing multiple mergers as a part of the evolution.

Keywords: infrared: galaxies – galaxies: high-redshift – galaxies: ISM – galaxies: evolution – galaxies: starburst – radio lines: ISM

1. INTRODUCTION

Most of the stellar mass in the Universe is assembled in the first few billion years of cosmic time, in the redshift range $1 \lesssim z \lesssim 3$ (see e.g., review by Madau & Dickinson 2014). Galaxies at this epoch typically have higher star formation rates (SFRs) compared to the present day. Among the high-z galaxy populations discovered, dusty star-forming galaxies (DSFGs) represent the most IR-luminous systems at this peak epoch. They are typically gas-rich, with molecular gas masses exceeding $M_{gas} = 10^{10} M_\odot$ and IR luminosities exceeding those of nearby (ultra-)luminous infrared galaxies (U/LIRG; $L_{IR} > 10^{11-13} L_\odot$; see reviews by Carilli & Walter 2013; Casey et al. 2014). Given the differences found between nearby ULIRGs and high-z DSFGs (e.g., Younger et al. 2010; Rujopakarn et al. 2011, 2013), studying their interstellar medium (ISM) properties, gas dynamics, and star-forming environments directly are essential to understanding how galaxies are initially assembled at early epochs.

In the classical model of disk galaxy formation (Fall & Efstathiou 1980), disk galaxies form out of the gas that is cooling off from the hot halos associated with dark matter (DM) potential wells while maintaining the specific angular momentum as the gas settles into rotationally supported disks (Mo et al. 1998). The structure and dynamics of disk galaxies are therefore closely correlated with the properties of their parent DM halos. Probing the structure and dynamics of disk galaxies at high redshift can thus inform us about the processes driving the assembly history of galaxies at early cosmic

tleung@astro.cornell.edu

[1] Department of Astronomy, Space Sciences Building, Cornell University, Ithaca, NY 14853, USA

[2] Center for Computational Astrophysics, Flatiron Institute, 162 Fifth Avenue, New York, NY 10010, USA

[3] Department of Physics and Astronomy, Rutgers, the State University of New Jersey, 136 Frelinghuysen Road, Piscataway, NJ, 08854-8019

[4] Astrophysics Group, Imperial College London, Blackett Laboratory, Prince Consort Road, London SW7 2AZ, UK

[5] Department of Physics and Astronomy, University of California, Irvine, CA 92697, USA

[6] European Southern Observatory, Karl-Schwarzschild-Straße 2, D-85748 Garching, Germany

[7] Institute for Astronomy, University of Edinburgh, Royal Observatory, Blackford Hill, Edinburgh EH9 3HJ, UK

[8] Institut de Radioastronomie Millimétrique (IRAM), 300 Rue de la Piscine, Domaine Universitaire de Grenoble, 38406 St. Martin d'Hères, France

[9] Institut d'Astrophysique de Paris, Centre national de la recherche scientifique (CNRS) & Université Pierre et Marie Curie (UPMC), 98 bis boulevard Arago, 75014 Paris, France

[10] Instituto de Astrofisica de Canarias, E-38200 La Laguna, Tenerife, Spain

[11] Departamento de Astrofisica, Universidad de La Laguna, E-38205 La Laguna, Tenerife, Spain

[12] Department of Physics and Astronomy, University of British Columbia, 6224 Agricultural Road, Vancouver, BC V6T 1Z1, Canada

[13] Centre for Extragalactic Astronomy, Department of Physics, Durham University, South Road, Durham, DH1 3LE, UK

[14] Physics Department, Lancaster University, Lancaster, LA1 4YB, UK

times. For instance, by tracing the gas dynamics, the Tully-Fisher relation (Tully & Fisher 1977), which links the angular momentum of the parent DM halo of a disk galaxy with the luminosity/mass of its stellar populations, can be studied out to earlier epochs. Past observations have led to two physical pictures for the nature and origin of DSFGs: compact irregular starbursts resulting from major mergers (of two or more disks) and extended disk-like galaxies with high SFRs (e.g., Tacconi et al. 2006, 2008; Shapiro et al. 2008; Engel et al. 2010; Riechers et al. 2010; Ivison et al. 2010a, 2011; Riechers et al. 2011a,c; Hodge et al. 2012; Riechers et al. 2013; Ivison et al. 2013; Bothwell et al. 2013; Riechers et al. 2014b; Hodge et al. 2015; Oteo et al. 2016a; Riechers et al. 2017) resulting from minor mergers and/or cold gas accreted from the intergalactic medium (IGM; also known as cold mode accretion; CMA; e.g., Kereš et al. 2005; Dekel et al. 2009a; Davé et al. 2010). However, as individual DSFGs can fall into either physical picture, a third interpretation is that DSFGs are a heterogeneous population composed of both compact starbursts and extended disks (e.g., Hayward et al. 2013), presumably observed at different stages of evolution. Determining their gas kinematics is therefore key to better understanding their formation mechanisms and shedding light on whether major mergers or continuous accretion dominate and sustain their intense star formation. However, such studies require high spatial resolution and sensitivity in order to image their gas reservoirs, and thus, are relatively expensive to carry out. To date, only a handful of high-z galaxies have been mapped in their molecular gas at high resolution, revealing a mixture of rotating disks and galaxy mergers (e.g., Swinbank et al. 2011; Hodge et al. 2012; Ivison et al. 2013; Oteo et al. 2016b, 2017a, 2018).

With the goal to better understand the star-forming conditions and the gas dynamics of high-z DSFGs, we observed multi-J CO and [CII] line emission in HerMES J022547-041750 (HXMM05; RA, Dec $= 02^\text{h}25^\text{m}47^\text{s}$, $-04°17'50''$; J2000), one of the brightest DSFGs known, at $\lesssim 0.''15$ resolution. Line emission from different rotational transitions of CO is useful for determining molecular gas mass and physical properties of the ISM. The [CII] ($^2P_{3/2} \rightarrow {}^2P_{1/2}$) fine-structure line at rest-frame 157.7 μm is one of the brightest emission lines in star-forming galaxies, and can contribute up to 1% of the FIR luminosity of galaxies (Malhotra et al. 1997; Nikola et al. 1998; Colbert et al. 1999). In addition, [CII] and CO ($J = 1 \rightarrow 0$) line emission trace similar gas kinematics in nearby star-forming galaxies (e.g., Mittal et al. 2011; Braine et al. 2012; Kramer et al. 2013; Pineda et al. 2013), making the former a powerful probe of high-z gas kinematics, especially when paired with the exceptional capabilities of the Atacama Large Millimeter/submillimeter Array (ALMA).

The target HXMM05 was discovered in the *Herschel* Multitiered Extragalactic Survey (HerMES; Oliver et al. 2012) as one of 29 high-z strongly-lensed galaxy candidates identified (Wardlow et al. 2013; Bussmann et al. 2015). The par-

ent sample was selected based on a flux density threshold of $S_{500} \geq 80$ mJy at 500 μm. The surface density of such bright DSFGs is (0.31 ± 0.06) deg^{-2} (Wardlow et al. 2013). Previous high-resolution imaging obtained with the *Hubble Space Telescope (HST)* and ALMA and lens modeling of $0.''4$ resolution dust continuum data at 870 μm show that HXMM05 is at most weakly lensed, with magnification factor $\mu_{870} \lesssim 1.4$ (Bussmann et al. 2015)[15]. HXMM05 is therefore intrinsically extremely IR-luminous, unlike other typically strongly-lensed DFSGs in the parent sample with similar sub-millimeter flux densities. Bussmann et al. (2015) find a total of three unlensed, intrinsically-bright DSFGs out of the parent sample of 29. This yields a surface density of $\sim$0.03 deg^{-2} for such sources, which makes them even rarer than strongly-lensed DSFGs. HXMM05 therefore belongs to a rare and understudied luminous/massive high-z galaxy population. Currently, the general consensus is these unlensed DSFG with $S_{500} \gtrsim 100$ mJy appear to be predominantly major galaxy mergers (e.g., HXMM01 and G09v124; Fu et al. 2013; Ivison et al. 2013). In this work, we investigate the nature of HXMM05 — to examine whether it is a dispersion-dominated merger, or an isolated HyLIRG. We securely determine its redshift to be $z = 2.9850$ through multi-J CO and [CII] line observations, indicating that HXMM05 is near the peak epoch of cosmic star formation.

This paper is structured as follows. In §2, we summarize the observations and procedures used to reduce the data. We also briefly describe the ancillary data used in our analysis. In §3, we present the main results. In §4, we present the results from spectral energy distribution (SED) modeling and dynamical modeling of the [CII] line data using the tilted-ring and "envelope"-tracing methods. In §5, we discuss the properties of HXMM05 and compare them to those of other galaxy populations. We discuss the key implications of our findings in §6, and summarize the main results and present our conclusions in §7. Throughout this paper, we use a concordance ΛCDM cosmology, with parameters from the WMAP9 results: $H_0 = 69.32$ km s^{-1} Mpc^{-1}, $\Omega_M = 0.29$, and $\Omega_\Lambda = 0.71$ (Hinshaw et al. 2013).

2. OBSERVATIONS AND ANCILLARY DATA

2.1. *Combined Array for Research in Millimeter-wave Astronomy (CARMA) CO ($J = 3 \rightarrow 2$)*

Based on the *Herschel*/SPIRE multi-band colors of $S_{500} < S_{250} < S_{350}$, we expected the redshift of HXMM05 to be $2 \lesssim z \lesssim 3.5$, and its CO ($J = 3 \rightarrow 2$) line — at rest-frame frequency $\nu_\text{rest} = 345.79599$ GHz — to be redshifted into the 3 mm receiver window of CARMA. We therefore performed a blind CO line search in HXMM05 with CARMA in the D array configuration. Five tracks were executed under

---

[15] The orientation of the *HST* image of HXMM05 shown in Figure 3 of Calanog et al. (2014); Bussmann et al. (2015) is incorrect (i.e., North is down instead of up), but the correct locations of all galaxies were used in the lens modeling.

Table 1
HXMM05 Observations Summary.

Observation	Telescope	Date	t_{on}	Bandpass	Flux	Gain	Ω_{beam} [a]	Array config.	ν
			(hr)		Calibrators		(major × minor, PA)		(GHz)
(1)	(2)	(3)	(4)	(5)	(6)	(7)	(8)	(9)	(10)
870 μm	SMA	25-Aug-2010	1.08	3C84	Uranus	J0238+166, J0217+017	0″99 × 0″78, −68.2°	Subcompact	342.017
		25-Sep-2010	2.06	3C454.3	Uranus, Callisto	—	—	Extended	342.003
		05-Aug-2011	2.93	3C454.3	Uranus, MWC349A	—	—	Extended	340.224
CO($J=3\rightarrow2$)	CARMA	02-Sep-2010	1.57	3C84	Uranus	J0239−025	7″68 × 5″00, −53°	D	89.9117
		03-Sep-2010	2.43	—	—	—	—	—	93.5887
		04-Sep-2010	2.09	—	—	—	—	—	103.3739
		05-Sep-2010	2.33	—	—	—	—	—	89.9115
		12-Sep-2010	1.65	—	—	—	—	—	107.0499
2.3 mm	PdBI	21-Sep-2010	0.8	B0215+015	MWC349	B0215+015	14″85 × 2″59, −35.8°	D	131.1
CO($J=5\rightarrow4$)		23-Sep-2010	0.6	3C454.3	—	—	—	—	145.4
		26-Sep-2010	0.6	—	—	—	7″43 × 4″08, 111.2°	—	145.4
CO($J=1\rightarrow0$)	VLA	20-Sep-2014	1.40	3C147	3C147	J0215−0222	1″21 × 0″80, 36°	DnC	Ka-band
		17-Nov – 11-Dec-2014	8.96	J0542+4951	J0542+4951	—	—	C	—
[CII]	ALMA 12 m [b]	15-Jun-2015	0.15	J2232+1143	Ceres	J0241−0815	0″18 × 0″14, 61.3°	21−784 [m]	472.661
		27-Aug-2015	0.15	J0224+0659	J0224+0659	J0241−0815	—	15−1574 [m]	472.665
CO($J=10\rightarrow9$)	ALMA ACA [c]	11-Sep-2017	0.45	J0006−0623	Uranus	J0217+0144	5″35 × 3″65, −85°	ACA	289.995
		16-Sep-2017	0.45	J0522−3627	—	—	—	—	—

Note. — Columns: (1) line or continuum wavelength observed; (2) telescope; (3) date of observations; (4) on-source time; (5−7) calibrators; (8) clean beam size (untapered); (9) array configuration or baseline range; (10) local oscillator frequency for observations obtained with the SMA, CARMA, and ALMA, or observed frequency for observations made with the PdBI and VLA.
[a] Synthesized beam size obtained with "natural" weighting and after combining all tracks of the same spectral setup.
[b] Cycle-2 data. For observation details of the ALMA cycle-0 data, see Bussmann et al. (2015).
[c] Cycle-4 data.

excellent weather conditions between 2010 September 02 and 21 (Program ID: cx310; PI: D. Riechers). A total of 10.1 hours of on-source time was obtained after combining all data. We scanned the 3 mm window using four distinct frequency setups, covering a frequency range of $\nu_{obs} = 84.98 - 111.97$ GHz. For each setup, the correlator provided sixteen spectral windows, each with a bandwidth of 494.792 MHz and 95 channels, resulting in an effective bandwidth of 3.75 GHz per sideband after accounting for overlapping edge channels. This correlator setup provides a spectral resolution of $\Delta\nu = 5.208$ MHz (i.e., $\Delta v = 18$ km s^{-1} at $\nu_{obs} = 86.8$ GHz). All tracks used the same calibrators, as summarized in Table 1. We estimate a flux calibration accuracy of $\sim 15\%$.

The MIRIAD package was used to calibrate the visibility data. The calibrated visibility data were imaged and deconvolved using the CLEAN algorithm with natural weighting, yielding a synthesized beam size of $7.''68 \times 5.''00$, at a position angle (PA) of $-53°$. The final rms noise is typically $\sigma_{ch} = 2.26$ mJy beam^{-1} over a channel width of 90 km s^{-1}. We form four continuum images at $\nu_{cont} = 90$, 93.4, 103, and 107 GHz, by averaging across the line-free channels in each setup (i.e., one per spectral tuning). The final rms of the continuum images are $\sigma_{cont} = 0.17$, 0.37, 0.33, and 0.43 mJy beam^{-1}, respectively.

2.2. *Plateau de Bure Interferometer (PdBI)*
CO (J = 5 → 4) and 131 GHz Continuum

We detected a single line in the CARMA data (see §3.1). Based on the SPIRE colors, the line is most likely CO($J=3\rightarrow2$), suggesting a redshift of $z \approx 2.985$ for HXMM05. This redshift was spectroscopically confirmed through the detection of a second CO line, which was observed with IRAM PdBI (Program ID: U–3; PI: N. Fiolet). Based on the redshift suggested by the CARMA data, we expected the CO ($J = 5 \rightarrow 4$) line ($\nu_{rest} = 576.26793$ GHz) to be redshifted to an observed frequency of $\nu_{obs} = 144.6093$ GHz. Observations were carried out in good weather conditions in the D array configuration with six antennas on 2010 September 23 and 26. A total on-source time of 1.4 hours was obtained in the combined tracks. The 2 mm receivers were used to cover the expected frequency of the CO ($J = 5 \rightarrow 4$) line and the underlying continuum. The WideX correlator was used, providing a spectral resolution of 1.95 MHz (about 4 km s^{-1} at ν_{obs}) over an effective bandwidth of 3.6 GHz, in dual polarization mode. Calibrators used for bandpass, flux, and complex gain calibrations are listed in Table 1. We estimate a flux calibration accuracy of 15%.

The GILDAS package was used to calibrate and analyze the visibility data. The calibrated visibility data were imaged and deconvolved using the CLEAN algorithm with natural weighting, yielding a synthesized beam of $7.''43 \times 4.''08$ at PA $= 111°$. The final rms noise is 5.53 mJy beam^{-1} over 20 MHz (41.3 km s^{-1}). A continuum image at an average frequency of $\nu_{cont} = 145.4$ GHz was produced by averaging over the line-free channels ($\Delta\nu = 3.12$ GHz), yielding an rms noise of 0.44 mJy beam^{-1}.

We also observed the $\nu_{obs} = 131.1$ GHz continuum emission in HXMM05 with the PdBI (Program ID: U–3; PI: N. Fiolet) to rule out an alternative redshift option. Observations were carried out on 2010 September 21 under good weather conditions in the D array configuration for 0.6 hours of on-source time (Table 1). The visibility data were calibrated using GILDAS. Imaging and deconvolution were performed using the CLEAN algorithm with natural weighting. We formed a continuum image by averaging across all channels within an effective bandwidth of 3.6 GHz, reaching an rms of $\sigma_{cont} = 0.21$ mJy beam^{-1} and a beam size of $14.''85 \times 2.''59$ at PA $= -36°$.

2.3. *NSF's Karl G. Jansky Very Large Array (VLA)*
CO (J = 1 → 0)

Based on the redshift determined from the CO($J=3\rightarrow2$) and CO ($J = 5 \rightarrow 4$) lines, we targeted the CO ($J = 1 \rightarrow 0$) line ($\nu_{rest} = 115.27120$ GHz) in HXMM05 using the the VLA, for a total of ten observing sessions (Program ID: 14B-302; PI: S. Bussmann). One session was carried out on 2014 September 20 in the DnC array configuration and the remaining nine sessions were carried out between 2014 November 17 and December 11 in the C array configuration, A total of 10.5 hours of on-source time was obtained in the combined ten sessions. The Ka-band receivers were used to cover the redshifted CO ($J = 1 \rightarrow 0$) line. The WIDAR correlator was used in full polarization mode, providing a total bandwidth of 2 GHz covered by sixteen sub-bands, each with a bandwidth of 128 MHz and a channel spacing of 2 MHz (29 km s^{-1}). Calibrators are listed in Table 1. We estimate a flux calibration accuracy of $\lesssim 15\%$.

Visibility data were calibrated and analyzed using version 4.7.1 of the CASA package. We combined all calibrated data and imaged the visibilities using the CLEAN algorithm with natural weighting to maximize sensitivity, yielding a synthesized beam size of $1.''21 \times 0.''80$ at PA $= 36°$. The final rms noise is 0.041 mJy beam^{-1} over 6 MHz (62 km s^{-1}), or 0.028 mJy beam^{-1} per $\Delta v = 145$ km s^{-1} velocity bin. A continuum image at $\nu_{cont} = 31.27$ GHz was produced by averaging over all the line-free channels, yielding an rms noise of $\sigma_{cont} = 3.19$ μJy beam^{-1}. To examine the kinematics of the CO ($J = 1 \rightarrow 0$) line emission at higher resolution, we made an additional line cube using Briggs weighting with robustness $R = 0.5$. An rms noise of $\sigma_{ch} = 0.031$ mJy beam^{-1} per velocity bin ($\Delta v = 145$ km s^{-1}) is reached in the resulting line cube, with a beam size of $0.''94 \times 0.''71$ at PA $= 31°$.

2.4. *ALMA [CII]*

We observed the [CII] fine-structure line ($\nu_{rest} = 1900.536900$ GHz) in HXMM05 with ALMA on 2015 June 15 and August 27 during Cycle 2 (ID: 2013.1.00749.S,

PI: D. Riechers). The [C II] line is redshifted to Band 8 at the redshift of HXMM05 determined from our CO data ($z = 2.9850$). We employed the frequency division mode (FDM) correlator setup with dual polarization, providing an effective bandwidth of 7.5 GHz and a spectral resolution of 1.95 MHz (1.2 km s^{-1}). The on-source time, baseline coverage, and calibrators used in each track are listed in Table 1. All data were calibrated manually due to the uncertain flux scale of Ceres, which was used as the flux calibrator in one of the two tracks. The calibrated amplitudes of both the phase and bandpass calibrators are consistent with those found in the ALMA Calibrator Source Catalogue. The flux scale was also verified by comparing the calibrated amplitudes of the same phase calibrator across the two tracks. We estimate a flux calibration accuracy of 15%.

All data were calibrated using CASA version 4.5.0 and were then combined, imaged, and deconvolved using the CLEAN algorithm with natural weighting, yielding a synthesized beam of $0.''18 \times 0.''14$ at PA $= 61.3°$. To obtain an optimal balance between sensitivity and spectral resolution, we binned the data cubes to spectral resolutions of $\Delta v = 25$ km s^{-1} and 300 km s^{-1}, reaching typical rms noise values of $\sigma_{ch} = 2.36$ and 0.75 mJy beam^{-1} per channel, respectively. A continuum image was obtained by averaging across the line-free channels and excluding any channels that were affected by atmospheric features. The bandwidth used to form the continuum images is 5.47 GHz, yielding an rms noise level of $\sigma_{cont} = 0.22$ mJy beam^{-1}.

We also imaged the visibilities with uv-tapering applied at 500 kλ (311.5 m) to recover potential diffuse low surface brightness emission and structure on larger spatial scales. After tapering, a line cube binned to a spectral resolution of $\Delta v = 150$ km s^{-1} was imaged and deconvolved using the CLEAN algorithm and natural weighting. We used the tapered data cube and image to define the apertures used for extracting the line and underlying continuum fluxes, and the line spectrum (see §3). The beam size for the tapered data is $0.''31 \times 0.''26$ at PA $= 69.5°$, which is roughly twice the untapered beam size. The final rms noise is $\sigma_{cont} = 0.33$ mJy beam^{-1} for the tapered continuum map, and $\sigma_{ch} = 1.25$ mJy beam^{-1} per 150 km s^{-1} bin for the data cube.

2.5. ALMA CO(J = 10→9)

In ALMA Cycle 4, we observed the CO($J = 10 \rightarrow 9$) line ($\nu_{rest} = 1151.98545200$ GHz) in HXMM05 on 2017 September 11 and 16 (ID: 2016.2.00105.S, PI: D. Riechers) using the 7 m Atacama Compact Array (ACA). The CO($J = 10 \rightarrow 9$) line is redshifted to Band 7 for HXMM05. We employed the time division mode (TDM) correlator setup with dual polarization, providing an effective bandwidth of 7.5 GHz and a spectral resolution of 15.6 MHz (16.2 km s^{-1}). The on-source time, baseline coverage, and calibrators of each track are listed in Table 1. We conservatively estimate a flux calibration accuracy of 15%.

All data were calibrated using version 5.1.1 of CASA, and were then combined, imaged, and deconvolved using the CLEAN algorithm with natural weighting. This yields a clean beam of $5.''35 \times 3.''65$ at PA $= -85°$. We binned the data cube to a spectral resolution of $\Delta v = 49$ km s^{-1}, reaching a typical rms noise of $\sigma_{ch} = 1.20$ mJy beam^{-1} per channel. A continuum image was obtained by averaging across the line-free channels over a bandwidth of 5.61 GHz, yielding an rms noise of $\sigma_{cont} = 0.37$ mJy beam^{-1}.

2.6. Ancillary Data
2.6.1. Herschel/SPIRE and PACS, and MAMBO 1.2 mm

HXMM05 was observed with *Herschel*/PACS and SPIRE at 100, 160, 250, 350, and 500 μm as part of the HerMES project (Oliver et al. 2012). HXMM05 remains undetected at 100 μm down to a 5σ limit of $S_{100} < 28.8$ mJy, but is detected at 160 μm. The 160 μm photometry was extracted from the Level 5 XMM-VIDEO3 data using a positional prior from the *Spitzer*/MIPS 24 μm catalog with aperture photometry, and with appropriate aperture corrections applied (PACS DR4). For the SPIRE photometry, we adopted the fluxes reported by Wardlow et al. (2013), which were extracted using STARFINDER (Diolaiti et al. 2000). We also include the 1.2 mm photometry obtained with the IRAM 30-m telescope/MAMBO in modeling the SED of HXMM05 (Wardlow et al. 2013; Table 2; see §4.1).

2.6.2. SMA 870 μm

We also make use of 870 μm continuum data obtained with the Submillimeter Array (SMA; IDs: 2010A-S091 and 2011A-S068, PIs: A. Cooray and S. Bussmann; Wardlow et al. 2013). Observations were carried out in the extended and subcompact array configurations on 2010 August 16 and September 25, and 2011 August 05, with local oscillator frequencies of 342.224 GHz and 342.003 GHz (extended), and 340.017 GHz (subcompact), respectively. The on-source time of each track is listed in Table 1. Uranus was used as the primary flux calibrator, and the quasars J0238+166 and J0217+017 were used as complex gain calibrators for all three tracks. Quasars 3C454.3 and 3C84 were used for bandpass calibration. MWC349A and Callisto were observed as secondary flux calibrators in the extended configuration tracks.

All visibility data were calibrated using the IDL-based MIR package and imaged using MIRIAD. We combined all tracks to form a continuum image using the CLEAN algorithm with natural weighting, yielding a synthesized beam of $0.''99 \times 0.''78$ at PA $= -68.2°$ and an rms noise of 0.92 mJy beam^{-1} over the full bandwidth of 7.5 GHz.

2.6.3. ALMA Cycle-0 870 μm

We previously observed the 870 μm continuum emission in HXMM05 with ALMA in Band 7 (ID: 2011.0.00539.S; PI: D. Riechers; also see Bussmann et al. 2015). Visibilities were imaged using the CLEAN algorithm with

Table 2
Photometry obtained for HXMM05.

Wavelength/Band (μm)	Frequency (GHz)	Flux Density		Instrument/Band
0.15	2000000	< 2.29	μJy	*GALEX*/FUV
0.23	1300000	< 2.29	μJy	*GALEX*/NUV
0.38	780000	< 0.19	μJy	CFHT/u^*
0.49	610000	< 0.14	μJy	CFHT/g'
0.63	480000	< 0.20	μJy	CFHT/r'
0.76	390000	< 0.24	μJy	CFHT/i'
0.88	340000	< 0.11	μJy	VISTA/Z-Band
0.89	340000	< 0.35	μJy	CFHT/z'
1.02	290000	< 0.31	μJy	VISTA/Y-Band
1.16	260000	< 0.10	μJy	*HST*/F110W
1.25	240000	< 0.35	μJy	VISTA/J-Band
1.65	180000	< 0.55	μJy	VISTA/H-Band
2.15	140000	< 0.78	μJy	VISTA/Ks-Band
3.4	88174	< 0.20	mJy	*WISE*/W1
3.6	83275	< 1.25	μJy	*Spitzer*/IRAC
4.5	66620	< 1.25	μJy	*Spitzer*/IRAC
4.6	65172	< 0.19	mJy	*WISE*/W2
5.8	51688	8.61 ± 1.54	μJy	*Spitzer*/IRAC
8.0	37474	8.14 ± 4.84	μJy	*Spitzer*/IRAC
12	24983	< 0.52	mJy	*WISE*/W3
22	13627	< 3.24	mJy	*WISE*/W4
24	12491	1.08 ± 0.02	mJy	*Spitzer*/MIPS
70	4283	< 10.8	mJy	*Spitzer*/MIPS
100	2998	< 17.3	mJy	*Herschel*/PACS
160	1874	< 90.0	mJy	*Spitzer*/MIPS
160	1874	86.3 ± 17.9	mJy	*Herschel*/PACS
250	1200	106 ± 7	mJy	*Herschel*/SPIRE
350	857	120 ± 10	mJy	*Herschel*/SPIRE
500	600	92.1 ± 7.6	mJy	*Herschel*/SPIRE
635	472	52.5 ± 5.9	mJy	ALMA
870	345	18.0 ± 0.4	mJy	ALMA
870	345	21.5 ± 3.1	mJy	SMA
1037	289	11.8 ± 0.8	mJy	ALMA ACA
1200	250	8.9 ± 0.9	mJy	MAMBO
2061.3	145.4	< 1.31	mJy	PdBI
2284.7	131.1	< 0.63	mJy	PdBI
2801.8	107	< 1.30	mJy	CARMA
2910.6	103	< 0.98	mJy	CARMA
3000 [a]	100	0.50 ± 0.11	mJy	CARMA
3209.8	93.4	< 1.11	mJy	CARMA
3331.0	90	< 0.50	mJy	CARMA
9586.8	31.3	0.0184 ± 0.00314	mJy	VLA

References. — *GALEX* limits are from XMM-LSS DIS (Pierre et al. 2004; Martin et al. 2005). CFHT limits are from CFHTLS-D1 (Chiappetti et al. 2005). VISTA limits are from the VIDEO survey (Jarvis et al. 2013). *HST* limit is taken from Calanog et al. (2014). Upper limits from *Spitzer*/IRAC and MIPS observations are the survey depths of SWIRE and SERVS (Lonsdale et al. 2003; Nyland et al. 2017). *Herschel*/PACS limit at 100 μm is obtained from Level 5 observations of the XMM-VIDEO3 field (Oliver et al. 2012). PACS 160 μm flux density is obtained from the DR4 PACS catalog of the XMM-VIDEO3 field. *Herschel*/SPIRE and MAMBO photometry are from Wardlow et al. (2013). ALMA 870 μm flux density is from Bussmann et al. (2015).

Note. — All upper limits are 3σ limits. Uncertainties on the SPIRE flux densities include those due to confusion noise. Uncertainties quoted here for the radio and mm interferometric measurements (i.e., with ALMA, CARMA, PdBI, SMA, and VLA) do not include those from absolute flux calibration (∼15%), which are accounted for in the SED modeling.

[a] Continuum emission measured in an image obtained by combining all four spectral setups covering the 3 mm window.

Briggs weighting (robustness $R = 0.5$), yielding a synthesized beam of $0.''50 \times 0.''40$ (PA $= 76.4°$) and an rms noise of $\sigma_{cont} = 0.28$ mJy beam^{-1}.

2.6.4. *Spitzer/IRAC and MIPS Near- and Mid-IR*

HXMM05 was observed with *Spitzer*/IRAC and MIPS as part of the *Spitzer* Wide-area InfraRed Extragalactic Survey (SWIRE; Lonsdale et al. 2003) in the XMM-LSS field. The survey depths (5σ) for point sources are $S_\nu < 3.7, 5.4, 48,$

and 37.8 μJy for the IRAC channels at 3.6, 4.5, 5.8 and 8.0 μm, respectively, and 230 μJy, 18 mJy, and 150 mJy for the MIPS bands at 24, 70, and 160 μm, respectively[16]. In the MIPS bands, HXMM05 is detected at 24 μm (SWIRE catalog DR2)[17]. The 24 μm photometry was extracted using aperture photometry and SEXTRACTOR (Savage & Oliver 2007). Appropriate aperture corrections have been applied. HXMM05 remains undetected at 70 and 160 μm; we adopt 3σ levels as the upper limits for the non-detections (see Table 2).

In the post-cryogenic period of *Spitzer*, more sensitive continuum images at 3.6 and 4.5 μm were obtained in the deeper *Spitzer* Extragalactic Representative Volume Survey (SERVS), which reaches 5σ limits of 1.25 μJy (Mauduit et al. 2012; Nyland et al. 2017). For the two SWIRE images observed at longer wavelengths (IRAC 5.8 and 8.0 μm), we perform aperture photometry to extract the fluxes of HXMM05 at the centroid position determined from the SMA 870 μm map. Final flux densities are reported in Table 2.

2.6.5. *Wide-field Infrared Survey Explorer (WISE) Near- and Mid-IR*

HXMM05 was observed with *WISE* as part of the ALLWISE program. Its flux density limits are reported in the ALLWISE source catalog available on the NASA/IRAC Infrared Science Archive (IRSA) and were extracted through profile-fitting. In Vega magnitude units, we find 15.460 ± 0.040, 14.905 ± 0.065, < 12.457, and < 8.817 for the four WISE bands (at 3.4, 4.6, 12, and 22 μm, respectively). The latter two are 3σ upper limits. Since a few sources with IR emission near HXMM05 are detected in the *Spitzer* images, we expect emission toward HXMM05 to be unresolved and blended within the *WISE* beam. As such, we adopt all the *WISE* fluxes as upper limits only, yielding 3σ limits of 0.20, 0.19, 0.52, and 3.24 mJy, respectively (Table 2).

2.6.6. *Visible and Infrared Survey Telescope for Astronomy (VISTA) Near-IR*

The XMM-LSS field was imaged with VISTA in the *Z*-, *Y*-, *J*-, *H*-, and *Ks*-bands as part of the VISTA Deep Extragalactic Observations (VIDEO) Survey (Jarvis et al. 2013), reaching 5σ limits of 25.7, 24.6, 24.5, 24.0, and 23.5 AB mag for a point source in a 2″ diameter aperture. HXMM05 is undetected in all bands. In Table 2, we report the corresponding 3σ levels as upper limits.

2.6.7. *CFHT UV-optical-IR*

HXMM05 was imaged with the CFHT/MegaCam in u^*, g', r', i', z' bands as part of the CFHT Legacy Survey Deep-1 field (CFHTLS-D1). In the final CFHTLS release (version T0007), the sensitivity limits corresponding to 80% completeness for a point source are 26.3, 26.0, 25.6, 25.4, and 25.0 AB mag

[16] http://swire.ipac.caltech.edu/swire/astronomers/program.html
[17] https://irsa.ipac.caltech.edu/data/SPITZER/SWIRE/docs/delivery_doc_r2_v2.pdf

for the five bands, respectively, or 3σ point-source sensitivities of 0.19, 0.14, 0.20, 0.24, 0.35 μJy. We show the $\sim 0.8''$ resolution CFHT deep field images retrieved from the CFHT Science Archive from the Canadian Astronomy Data Centre (CADC) in the Appendix. HXMM05 remains undetected in all bands according to the T0007 CFHTLS-Deep catalog (Hudelot et al. 2012; Table 2).

2.6.8. *Galaxy Evolution Explorer (GALEX) Near and Far-UV*

UV emission in the HXMM05 field was observed with *GALEX* in the FUV-1500 and NUV-2300 bands as part of the XMM-LSS Deep Imaging Survey (DIS). HXMM05 was covered in the XMMLSS_00 tile, which was observed for 75262 and 60087 seconds in the NUV and the FUV bands, respectively[18], reaching 3σ limits of 25.5 in AB mag (Pierre et al. 2004; Martin et al. 2005).

2.6.9. *XMM-Newton X-ray*

HXMM05 is located in the CFHTLS-D1 field, which was observed with the European Photon Imaging Camera (EPIC) onboard *XMM-Newton* for an integration time of around 20 ks in the *XMM* Medium Deep Survey (XMDS; Chiappetti et al. 2005), reaching 3σ point source limits of 3.7×10^{-15} erg s^{-1} cm^{-2} and 1.2×10^{-14} erg s^{-1} cm^{-2} in the soft (0.5−2 keV) and hard (2−10 keV) X-ray bands, respectively. These limits correspond to $L_{X,0.5-2\text{keV}} < 7.4 \times 10^{43}$ erg s^{-1} (soft) and $L_{X,2-10\text{keV}} < 9.5 \times 10^{44}$ erg s^{-1} (hard) at $z = 2.9850$, which reach the levels of powerful Seyfert galaxies (Elvis et al. 1978). HXMM05 remains undetected in these observations.

3. RESULTS

3.1. *CO Line Emission and Redshift Identification*

From the first two CO lines we detected — CO $(J = 3 \to 2)$ and CO $(J = 5 \to 4)$ with CARMA and the PdBI — we spectroscopically determine the redshift of HXMM05 to be $z = 2.9850 \pm 0.0009$. The CO$(J = 3 \to 2;$ $5 \to 4;$ $10 \to 9)$ lines remain spatially unresolved, and are detected at $> 8\sigma$, $> 6\sigma$, and $> 5\sigma$ significance, respectively (Figures 1 and 2). Due to the near-equatorial declination of HXMM05 and the sparse *uv*-sampling of the data, the PdBI synthesized beam is highly elongated, and the image fidelity is heavily affected by strong sidelobes. We fit single Gaussian profiles to the line spectra, as shown in Figure 1. The resulting best-fit parameters are summarized in Table 3. We note that given the broad linewidths observed up to the $J = 10 \to 9$ transition, the lack of emission at $v > 0$ km s^{-1} in the CO $(J = 5 \to 4)$ line may be attributed to the limited S/N of the data. The true CO $(J = 5 \to 4)$ flux may be a factor of two higher.

Upon determining the redshift of HXMM05, we observed the CO $(J = 1 \to 0)$ line with the VLA. We detect marginally spatially-resolved CO $(J = 1 \to 0)$ line emission at $> 14\sigma$ peak significance (Figure 2). The emission centroid is centered at
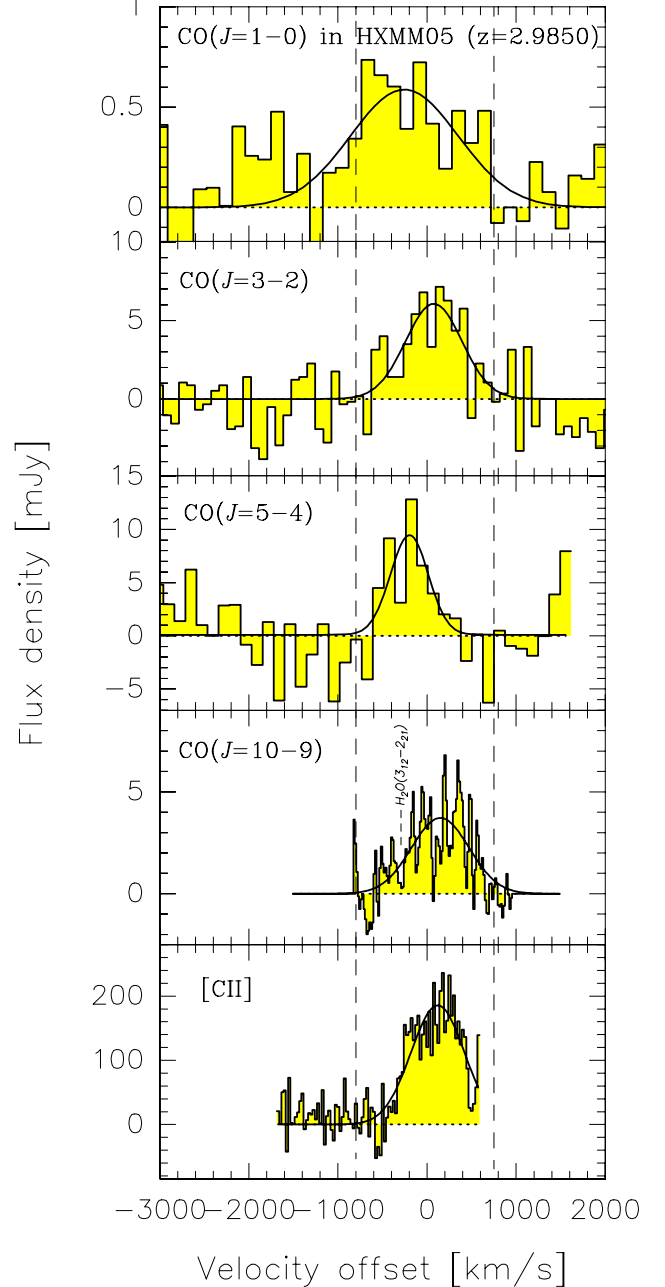
[18] Based on the images and catalog released in GR6.

Figure 1. Top to bottom: VLA CO $(J = 1 \to 0)$, CARMA CO $(J = 3 \to 2)$, PdBI CO $(J = 5 \to 4)$, and ALMA CO $(J = 10 \to 9)$ and [CII] line spectra (histograms) observed toward HXMM05. [CII] emission at $v \gtrsim 500$ km s^{-1} is dominated by noise near the edge of the spectral window, where a strong atmospheric feature is present. The spectral resolutions are $\Delta v = 145$, 90, 124, 16, and 25 km s^{-1} from top to bottom. CO $(J = 1 \to 0)$ and [CII] line spectra are same as those shown in Figure 3. Solid black lines show the best-fit single Gaussians. Vertical dashed lines are shown to facilitate linewidth comparison across panels. The redshifted frequency of the H$_2$O$(3_{12} \to 2_{21})$ line is annotated on the CO $(J = 10 \to 9)$ spectrum.

the position of HXMM05, but shifts from NW to SE with increasing velocity. A second peak is detected at $2.''6$ NE of HXMM05, at 6σ significance in the blueshifted channels (see Figure 2), corresponding to a projected separation of 20 kpc. In the subsequent sections of this paper, this NE component is referred to as X-NE, and the main component is referred to

Table 3
Parameters from fitting single Gaussians to the CO and [CII] line profiles and intensity maps shown in Figures 1, 2, 3, and 4.

Line	S_{peak} (mJy)	FWHM (km s^{-1})	I (Jy km s^{-1})	Deconvolved source size at FWHM (arcsec×arcsec, deg)	(kpc)	S_{cont} (mJy)
CO($J=1\rightarrow0$)[a]	0.55 ± 0.11	1118 ± 307	0.65 ± 0.22	—	—	(0.07 ± 0.03)[c]
X-Main	0.44 ± 0.07	1100 ± 210	0.51 ± 0.13	$1.12 \pm 0.37 \times 0.81 \pm 0.45, 173 \pm 49$[b]	8.8×6.4	(0.05 ± 0.02)[c]
X-NE	0.26 ± 0.04	718 ± 130	0.20 ± 0.05	$1.12 \pm 0.41 \times 0.26 \pm 0.42, 72 \pm 37$[b]	8.8×2.0	(0.02 ± 0.01)[c]
CO($J=3\rightarrow2$)	6.21 ± 0.98	791 ± 157	5.21 ± 1.32	——	—	(0.23 ± 0.26)[c]
CO($J=5\rightarrow4$)	9.38 ± 2.49	500 ± 159	4.97 ± 2.06	—	—	(0.16 ± 0.43)[c]
CO($J=10\rightarrow9$)	3.72 ± 0.23	760 ± 55	3.01 ± 0.29	—	—	—[d]
[CII]	183 ± 10	687 ± 53	133 ± 12	$0.91 \pm 0.08 \times 0.75 \pm 0.07, 29 \pm 17$	7.2×5.9	—[d]

Note. — The higher-J CO lines are unresolved.
[a] Emission from both X-Main and X-NE.
[b] Only marginally resolved.
[c] Not detected.
[d] Continuum emission was subtracted from the line cubes before extracting the spectrum.

Table 4
Continuum flux densities and deconvolved source sizes.

Instrument/Component	Wavelength (μm)	S_{peak} (mJy beam^{-1})	S_{total} (mJy)	Deconvolved source size at FWHM (arcsec×arcsec, deg)	(kpc)
ALMA Total	635	5.61 ± 0.22	52.5 ± 5.9	—	—
XD1 peak		4.95 ± 0.38	28.1 ± 2.4	$0.39 \pm 0.05 \times 0.36 \pm 0.05, 17 \pm 87$	3.1×2.8
XD2 peak		2.75 ± 0.28	15.7 ± 1.8	$0.39 \pm 0.06 \times 0.35 \pm 0.06, 174 \pm 89$	3.1×2.8
ALMA	870	10.61 ± 0.35	17.96 ± 0.43	$0.62 \pm 0.02 \times 0.54 \pm 0.02, 85 \pm 10$	4.9×4.2
SMA	870	12.8 ± 1.2	21.5 ± 3.1	$0.75 \pm 0.23 \times 0.66 \pm 0.27, 112 \pm 89$	5.9×5.2
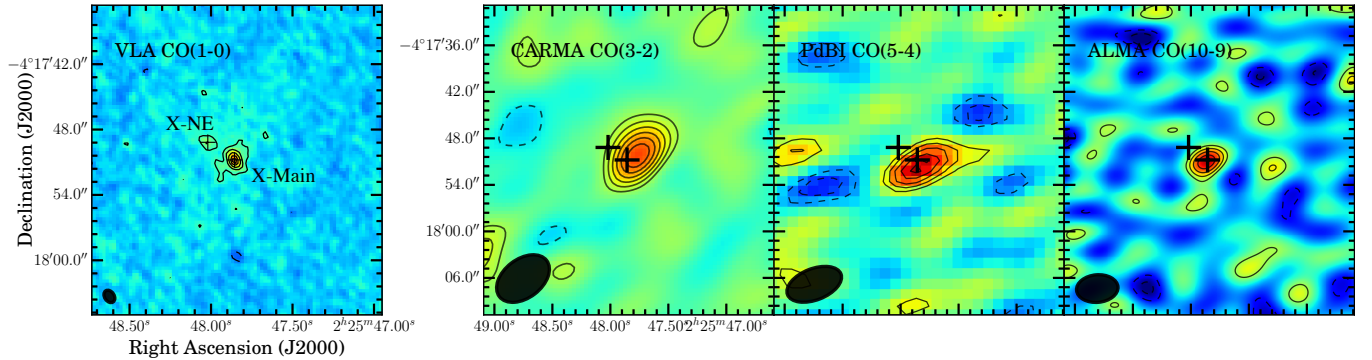
Figure 2. Left to right: Intensity maps of VLA CO($J=1\rightarrow0$), CARMA CO($J=3\rightarrow2$), PdBI CO($J=5\rightarrow4$), and ALMA ACA CO($J=10\rightarrow9$) line emission. Contours in the first panel are shown in steps of $[-3, 3, 6, 9, 12, 14, 15] \times \sigma_{1-0}$, where $\sigma_{1-0} = 14$ mJy km s^{-1} beam^{-1}. For the remaining panels, contours are shown in steps of $[-3, -2, 2, 3, 4, 5, 6, 7, 8] \times \sigma$, where $\sigma_{3-2} = 0.53$ Jy km s^{-1} beam^{-1} for CO($J=3\rightarrow2$), $\sigma_{5-4} = 0.73$ Jy km s^{-1} beam^{-1} for CO($J=5\rightarrow4$), and $\sigma_{10-9} = 0.63$ Jy km s^{-1} beam^{-1} for CO($J=10\rightarrow9$). Black markers indicate the positions of X-Main and X-NE as observed in CO($J=1\rightarrow0$) emission. Beam sizes are shown in the lower left corners and are summarized in Table 1.

as "X-Main".

We extract a spectrum using an aperture defined by the 2σ contours centered at the coordinates of HXMM05 (middle left panel of Figure 3), and a spectrum for just X-NE (bottom left panel of Figure 3). The centroid of X-NE is blueshifted by -535 ± 55 km s^{-1} with respect to X-Main. Assuming that the line detected is CO($J=1\rightarrow0$), the redshift of X-NE would be $z = 2.9779 \pm 0.0007$. We also extract a spectrum for the HXMM05 system as a whole, including emission from both X-Main and X-NE (top panel of Figure 1 and top left

panel of Figure 3). The best-fit linewidths and intensities are listed in Table 3. The CO($J=1\rightarrow0$) line is remarkably broad (>1100 km s^{-1} FWHM) and shows a hint of a double-horned profile, which likely results from contributions from both X-Main and X-NE (see Figure 3).

We fit 2D Gaussians to the two components detected in the velocity-integrated line intensity map, finding a deconvolved source size of $(1.''12 \pm 0.''37) \times (0.''81 \pm 0.''45)$ at PA $= 173 \pm 49°$ for HXMM05. This corresponds to a physical diameter of 8.8 kpc $\times 6.4$ kpc at $z = 2.9850$. For

the NE component, we find a deconvolved source size of $(1''12 \pm 0''41) \times (0''26 \pm 0''42)$ at PA $= 72 \pm 37°$, which corresponds to a physical size of 8.8 kpc × 2.0 kpc at $z = 2.9779$. The extent of the cold molecular gas in both HXMM05 and the NE component are consistent with those observed in other DSFGs (e.g., Ivison et al. 2011; Riechers et al. 2011a).

3.2. *[CII] Line Emission*

We detect spatially resolved [CII] line emission toward HXMM05 at a peak significance of $>13\sigma$ (in a tapered intensity map). At the full spatial resolution of the data (0''15), HXMM05 is resolved over >25 beams. To better determine the line profile shape, we create two [CII] line cubes — with and without *uv*-tapering (see §2). The 635 μm continuum emission has been subtracted from both line cubes in the *uv*-plane. We collapse them to form velocity-integrated line intensity (i.e., zeroth moment) maps as shown in Figure 4. We show the [CII] line spectrum of HXMM05 in the last panel of Figure 1 and the top right panel of Figure 3. The best-fit parameters obtained from fitting a single-Gaussian are listed in Table 3, together with those derived for the CO lines.

We extract separate spectra for X-Main and X-NE from the high resolution data cube using an aperture defined by the 1σ contours of the *tapered* intensity map. The resulting spectrum of X-Main is shown in the middle right panel of Figure 3. Fitting a single Gaussian yields a peak flux density of $S_{\rm peak} = 172 \pm 8$ mJy, a line FWHM of $\Delta v = 667 \pm 46$ km s^{-1}, and a line intensity of $I = 122 \pm 10$ Jy km s^{-1}. We also fit a double-Gaussian profile, yielding best-fit peak fluxes of $S_{\rm peak} = 53 \pm 30$ and 164 ± 10 mJy, and line FWHMs of $\Delta v = 167 \pm 85$ and 659 ± 101 km s^{-1}, respectively. The peaks are separated by $\Delta v_{\rm sep} = 346 \pm 124$ km s^{-1}. X-NE is detected at $\sim 6\sigma$ significance (see bottom right panel of Figure 3 and also Figure 4). We fit a 2D Gaussian to the tapered intensity map of X-Main, which yields a deconvolved FWHM source size of $(0''91 \pm 0''08) \times (0''75 \pm 0''07)$, or a physical size of $(7.2 \pm 0.6) \times (5.9 \pm 0.6)$ kpc, consistent with the extent seen in the higher resolution image.

The first and second moment maps of the [CII] emission representing the velocity and the velocity dispersion of X-Main along the line-of-sight (LOS) are shown in Figure 5. Moment maps are created from the line cube after clipping at $3\sigma_{\rm ch}$ per channel. Structures on the scale of the angular resolution ($\lesssim 1.2$ kpc) are seen in the channel maps (see Appendix §A). A velocity gradient along the NW-to-SE direction, varying over a velocity range of $\Delta v \simeq 600$ km s^{-1}, is seen in the velocity field (Figure 5). The dispersion map is remarkably uniform across the whole galaxy, with $\sigma_v \simeq 75$ km s^{-1}, except in the central $\lesssim 0''2$ region, where the dispersion reaches its peak at $\sigma_v \simeq 200$ km s^{-1}.

A position-velocity (PV) diagram extracted along the major kinematic axis of X-Main (see §4.2.1) is shown in Figure 6. The rising part of a rotation curve and the outer envelope are both detected. The latter is usually more pronounced in more inclined disks (as seen in nearby galaxies; see review by Sofue & Rubin 2001). The PV diagram is consistent with broad [CII] line emission, which varies by > 700 km s^{-1} within about 9 kpc.

We find comparable deconvolved source sizes for CO $(J = 1 \rightarrow 0)$ and [CII] emission (see Table 3), as confirmed by the comparable extents found after convolving the high resolution [CII] data to the CO $(J = 1 \rightarrow 0)$ line resolution (Figure 7). At the resolution of the VLA data, the velocity gradient seen in the CO $(J = 1 \rightarrow 0)$ line emission is consistent with that of the [CII] line, but more sensitive and higher angular resolution data are required to match the detailed velocity structures of both lines.

3.3. *H_2O Line Emission*

The H_2O $(1_{11} \rightarrow 0_{00}; 3_{12} \rightarrow 2_{21})$ lines at redshifted frequencies of 279.383 and 289.367 GHz are covered by the ALMA CO $(J = 10 \rightarrow 9)$ line observations. We do not detect the ground state H_2O line in emission or absorption down to a 3σ limit of < 0.80 Jy km s^{-1} beam^{-1}, assuming the same linewidth as the CO $(J = 10 \rightarrow 9)$ line (760 km s^{-1}). The $H_2O(3_{12} \rightarrow 2_{21})$ line is next to the CO $(J = 10 \rightarrow 9)$ line and is at most weakly detected; we conservatively report a 3σ upper limit of < 0.87 Jy km s^{-1} beam^{-1}, assuming the same linewidth as for the CO $(J = 10 \rightarrow 9)$ line.

3.4. *Continuum*

We show the *Spitzer*/IRAC images in Figure 8. Sources near HXMM05 are detected in the IRAC IR and CFHT NUV bands (see also Appendix §B), but HXMM05 remains undetected.

Among the four 3 mm spectral setups of the CARMA observations, we do not detect continuum emission in the individual tunings. A final continuum image created by averaging across all the tunings yields a weak detection at 4σ significance (see Table 2). In the PdBI 2 mm setups, continuum emission remains undetected. On the other hand, we detect Ka-band continuum emission underlying the CO $(J = 1 \rightarrow 0)$ line at 31.3 GHz at $\gtrsim 5\sigma$ significance, which remains unresolved at the resolution and sensitivity of the VLA data (Figure 7, see Table 2). The centroid of the 31.3 GHz continuum emission coincides with that of the CO $(J = 1 \rightarrow 0)$ line emission, and its flux density is consistent with that obtained from fitting a four-parameter model (Gaussian plus a first order polynomial) to the CO $(J = 1 \rightarrow 0)$ line spectrum extracted at the peak pixel. We also detect unresolved continuum emission at observed-frame ~ 1 mm (rest-frame 260 μm) underlying the CO $(J = 10 \rightarrow 9)$ line at $\sim 15 \sigma$ significance (Table 2).

Continuum emission underlying the [CII] line at observed-frame 635 μm is detected at a peak significance of $>31\sigma$ (see Table 2). Two dust peaks, separated by 2.4 kpc, are detected at high significance. One peak coincides with the 870 μm emission centroid (Figure 8) and with the CO $(J = 1 \rightarrow 0)$ emission
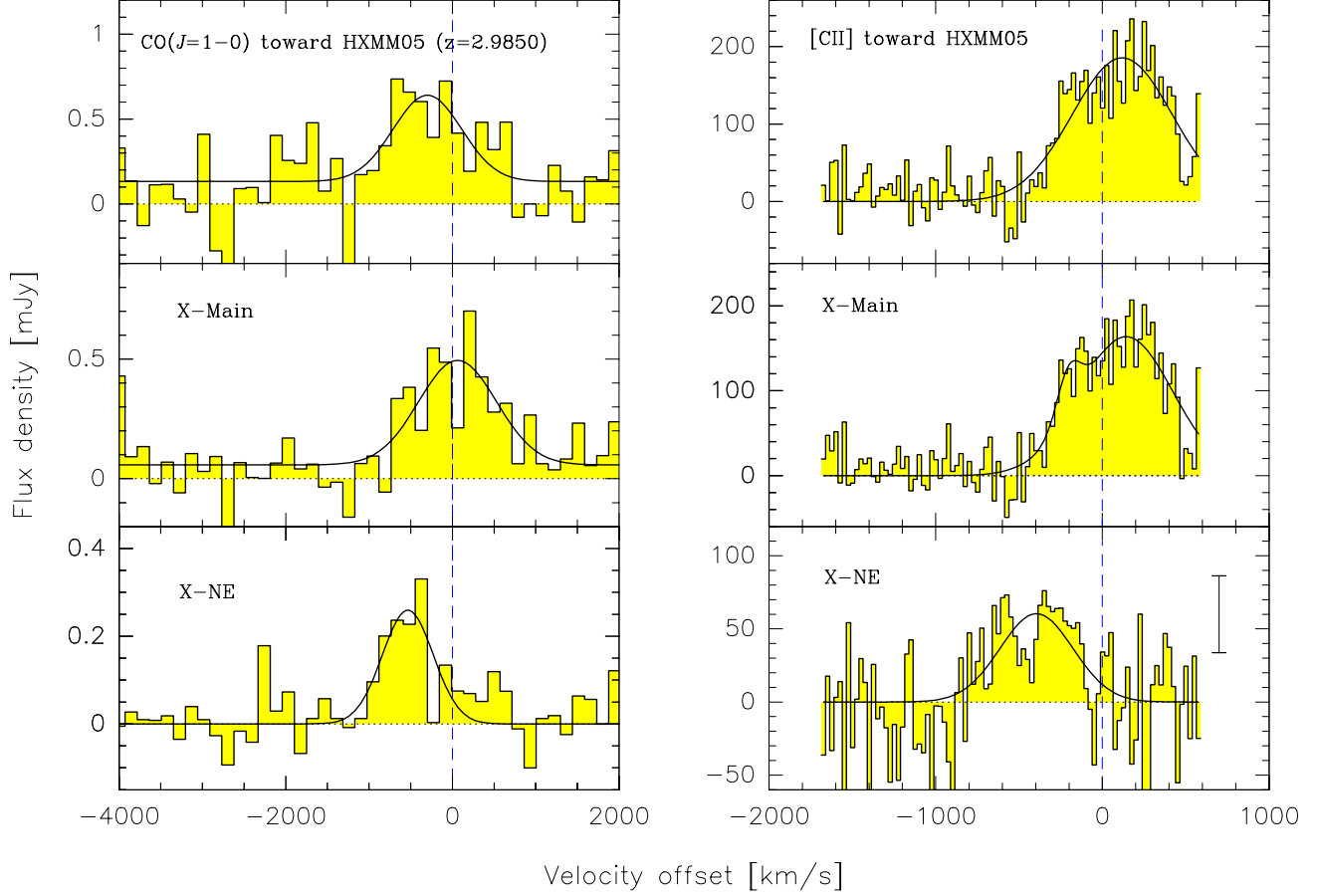
Figure 3. VLA CO($J=1{\to}0$) (left column) and ALMA [CII] (right column) spectra (histograms) of HXMM05. Top panels: Spectra of HXMM05, including emission from X-Main (middle panels) and X-NE (bottom panels). A typical error bar for the [CII] spectrum extracted for X-NE is shown in the bottom right panel. Vertical dashed lines mark a common $v = 0\,\mathrm{km\,s^{-1}}$ to facilitate comparison of line shapes and widths across panels. Spectral resolutions of the CO($J=1\to0$) and [CII] lines are $\Delta v = 145$ and $25\,\mathrm{km\,s^{-1}}$, respectively. Continuum underlying the [CII] line has been subtracted in the uv-plane. To account for the weakly detected Ka-band continuum in the VLA data, we fit models of a Gaussian and a zeroth order polynomial to the CO spectra (black lines). For the [CII] spectra, we fit single- (top and lower right) and double- (middle right) Gaussians. The velocity scale is with respect to $z = 2.9850$ (dashed lines). X-NE is detected in both CO($J=1\to0$) and [CII] lines at $\gtrsim 6\sigma$ significance (see Figures 2 and 4).
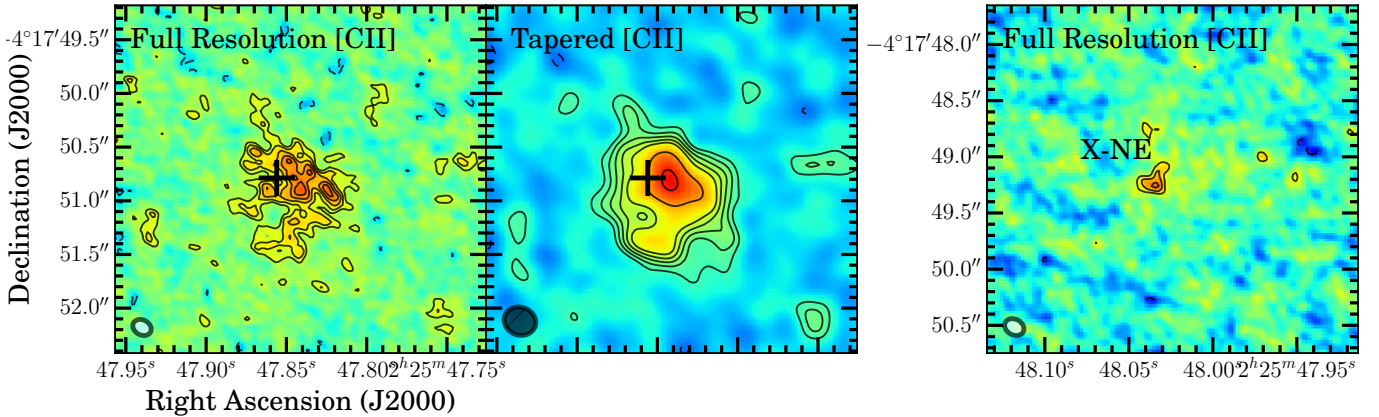
Figure 4. [CII] intensity maps at resolutions of $0\!\!''\!15$ (1.2 kpc; left and right panels) and at $0\!\!''\!3$ (tapered; middle panel). The left and middle panels show maps formed by integrating over velocity channels between $\Delta v \in [-226.9, 413.6]\,\mathrm{km\,s^{-1}}$. Contours are shown in steps of $[-3, -2, 2, 3, 4, 5, 6, 9, 12, 15]\times \sigma$, where $\sigma = 0.63\,\mathrm{Jy\,km\,s^{-1}\,beam^{-1}}$ (full resolution) and $\sigma = 0.68\,\mathrm{Jy\,km\,s^{-1}\,beam^{-1}}$ (tapered). Black crosses indicate the centroid position of CO($J=1\to0$) emission detected in X-Main (see Figures 2 and 7). The right panel shows a map of X-NE, formed by integrating over $\Delta v \in [-654.0, -136.4]\,\mathrm{km\,s^{-1}}$. Contours are shown in steps of $[-3, 3, 4, 5, 6]\times\sigma$, where $\sigma = 0.38\,\mathrm{Jy\,km\,s^{-1}\,beam^{-1}}$. Synthesized beam sizes of $0\!\!''\!18 \times 0\!\!''\!14$, PA $= 61.3°$ (untapered) and $0\!\!''\!31 \times 0\!\!''\!26$, PA $= 69.5°$ (tapered) are shown in the lower left corners of the panels.
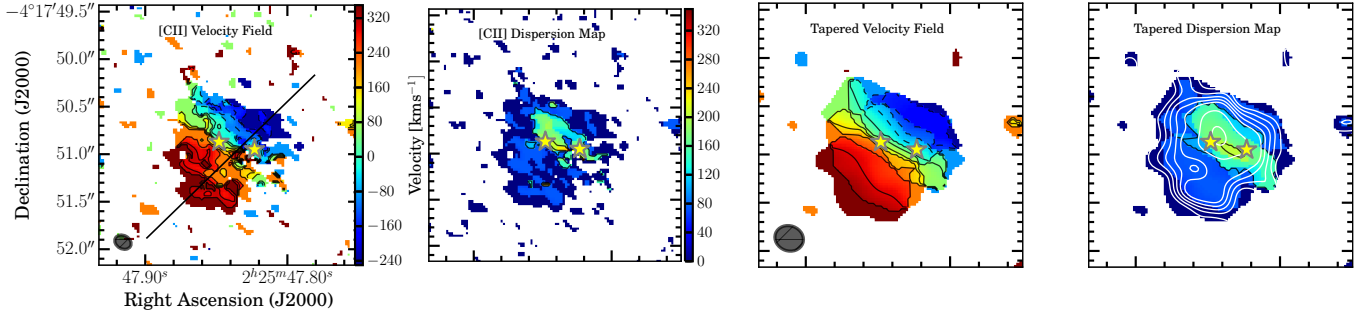
Figure 5. [CII] velocity field and dispersion maps, centered at X-Main. Contours in the velocity field maps start at $v = -236\,\mathrm{km\,s^{-1}}$ and increase to $364\,\mathrm{km\,s^{-1}}$ in steps of $50\,\mathrm{km\,s^{-1}}$. Black contours in the dispersion maps are shown in steps of $\Delta v = 100\,\mathrm{km\,s^{-1}}$. Tapered velocity-integrated [CII] line emission (white contours; same as right panel of Figure 4) is overlaid on the dispersion map in the last panel. Synthesized beams are shown in the lower left corners of the first and third panels: $0\rlap{.}''18 \times 0\rlap{.}''14$ for untapered (left) and $0\rlap{.}''31 \times 0\rlap{.}''26$ for tapered [CII] emission (right). Black line in the first panel shows the kinematic major axis, along which the PV slice shown in Figure 6 is extracted. Color-scales shown for the full resolution and tapered first and second moment maps are the same, respectively. Yellow star symbols indicate dust peaks detected at $635\,\mu\mathrm{m}$ (i.e., XD1 and XD2). A velocity gradient along the NW-SE direction is seen. The velocity dispersion is remarkably uniform across the galaxy, except at the central region, where it peaks at $\sigma_v \simeq 200\,\mathrm{km\,s^{-1}}$. X-NE is outside the field of view shown here.
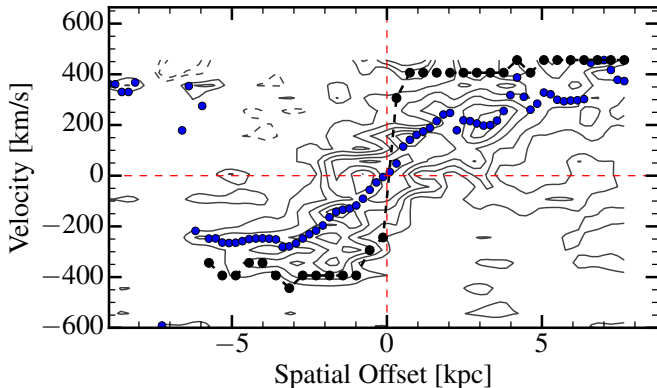
Figure 6. Rotation curve obtained from envelope-tracing (black dots and dashed line) overplotted on a [CII] PV diagram (contours) extracted along the major axis (see black line shown in the first panel of Figure 5). Velocities shown on the y-axis are observed (i.e., uncorrected for inclination). Blue markers show the centroid velocities of the spectra extracted at different spatial positions (see text in §4.2.2). Red dashed lines show the central position (vertical) and velocity (horizontal) determined from ROTCUR and from fitting a double-Gaussian to the [CII] spectrum.

centroid of X-Main (see Figure 7), whereas the other dust peak is offset to the SW (we denote these as XD1 and XD2, respectively, hereafter). We measure the total continuum flux density using an aperture defined by the 1σ contours. We fit a two-component 2D Gaussian to the continuum image and find deconvolved source sizes of $(0.''39 \pm 0.''05) \times (0.''36 \pm 0.''05)$ for XD1 and $(0.''39 \pm 0.''06) \times (0.''35 \pm 0.''06)$ for XD2, corresponding to physical sizes of about 3 kpc for both components. Since the deconvolved source sizes are larger than the beam size, the size measurements are not limited by the resolution of the observations. The peak flux densities are 4.95 ± 0.38 mWy beam^{-1} for XD1 and 2.75 ± 0.28 mJy beam^{-1} for XD2 (Table 4). Based on their total flux densities and sizes, their brightness temperatures in the Rayleigh-Jeans limit are 1.12 and 0.63 K, respectively, corresponding to $T_{\rm B,RJ} = 4.5$ and 2.5 K in the rest-frame.

We overplot the 635 μm continuum emission with the SMA and ALMA data observed at 870 μm in Figure 8. We fit a single-component elliptical Gaussian model to each of the 870 μm images. Only XD1 is detected at 870 μm. We also convolve the 635 μm data to the native resolution of the ALMA 870 μm data, and find a spatial offset between two peaks emission centroids. The emission centroids are determined by fitting a two-component Gaussian model to the 635 μm data and a single component Gaussian model to the 870 μm data. We thus conclude that XD2 is likely to be much fainter than XD1 at 870 μm, in order for it to remain undetected down to a 3σ limit of 0.84 mJy beam^{-1}.

While the [CII] emission shows a monotonic velocity gradient (Figure 5), which suggests that HXMM05 is a rotating disk with ordered motions, the dust continuum is almost exclusively produced at the two peaks embedded within the kpc-scale [CII] disk (Figure 8). Likely due to the limited surface brightness sensitivity of our observations, the [CII] line emission appears more irregular compared to the continuum.

We detect low surface brightness emission in the outer region of the 635 μm dust continuum map, which is consistent with the overall extent of the [CII] and CO $(J = 1 \rightarrow 0)$ emission (Figures 7 and 8). This diffuse component is likely to be more optically thin compared to XD1 and XD2, which likely dominate the dust optical depth estimated at 635 μm based on the integrated SED model (see §4.1), given that they contribute $>80\%$ to the total continuum flux at this wavelength. X-NE (which is detected in CO and [CII] line emission) is also weakly detected in the continuum at 635 μm at $>3\sigma$ significance, and in the UV, optical, and NIR wavebands (see the last two panels of Figure 7, Figure 8, and Figure 18 in Appendix §B).

4. ANALYSIS

4.1. *Spectral Energy Distribution Modeling*

We use the extensive multi-wavelength photometric data available in the XMM-LSS field to determine the IR, dust, and stellar properties of HXMM05 via SED modeling. Previously, Wardlow et al. (2013) modeled the dust SED of HXMM05 by fitting a simple modified blackbody to the photometry measured at (sub-)mm wavebands (*Herschel*-SMA-MAMBO), assuming a dust emissivity index of $\beta = 1.5$. This model suggests an IR luminosity (rest-frame $\lambda_{\rm rest} = 8 - 1000\,\mu$m) of $L_{\rm IR} = (3.2 \pm 0.4) \times 10^{13}\,L_\odot$ and a dust temperature of $T_d = (45 \pm 1)$ K. Here, we update the SED with more photometric data obtained since, covering UV through radio wavelengths (see Table 2). We model the observed dust SED using a modified blackbody (MBB) and the full SED using the MAGPHYS code (da Cunha et al. 2015) to derive a stellar mass in a self-consistent way from the dust and stellar emission.

4.1.1. *Modified Blackbody Model*

We model the dust SED of HXMM05 by assuming a single-temperature modified blackbody, which is parameterized by the characteristic dust temperature T_d. We fit MBB-based SED models to 16 photometric points covering rest-frame IR-to-mm wavelengths (observed-frame $24\,\mu$m-3 mm; see Table 2) using the code MBB_EMCEE (e.g., Riechers et al. 2013; Dowell et al. 2014). To account for the absolute flux-scale uncertainties associated with the photometry obtained with ALMA, SMA, PdBI, and CARMA, we add in quadrature an additional 15% uncertainty. The model consists of a MBB component that accounts for the FIR emission and a power-law component blue-ward thereof to describe the warmer dust emission at mid-IR wavelengths. The dust optical depth (as a function of wavelength) is taken into account via the parameter λ_0, where dust emission at $\lambda < \lambda_0$ (rest-frame) is optically thick ($\tau_\nu > 1$). The dust mass is calculated using

$$M_d = S_\nu\, D_L^2\, [(1+z)\, \kappa\, B_\nu(T)]^{-1}\, \tau_\nu\, [1 - \exp(-\tau_\nu)]^{-1}, \quad (1)$$

where D_L is the luminosity distance and B_ν is the Planck function. In estimating the dust mass, we assume an absorption mass coefficient of $\kappa = 2.64\,{\rm m^2\,kg^{-1}}$ at $\lambda = 125.0\,\mu$m (Dunne
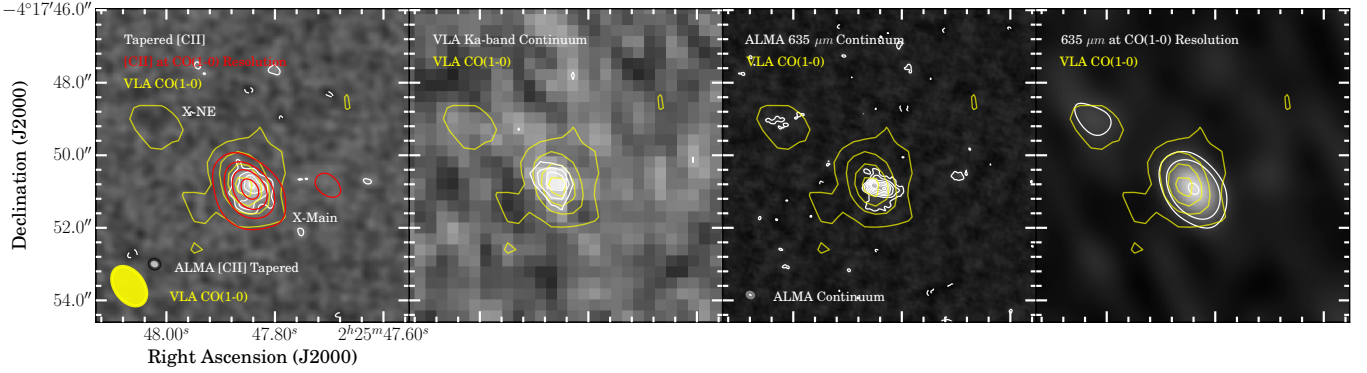
Figure 7. Left to right: VLA CO($J = 1 \rightarrow 0$) line emission (yellow contours) overlaid on ALMA [CII] line emission (first panel; integrated over line FWHM of X-Main), and continuum emission at 31.3 GHz and at 635 μm (last two panels). Contours of CO and [CII] line emission are shown in steps of $[-3, 3, 6, 9, 12, 14, 15] \times \sigma$, where $\sigma = 15.3$ mJy km s^{-1} beam^{-1} for the CO line, 0.676 Jy km s^{-1} beam^{-1} for the tapered [CII] (grayscale in the first panel), and 3.8 Jy km s^{-1} beam^{-1} for [CII] convolved to the same resolution as CO (red contours). Contours for the 635 μm continuum emission are shown in steps of $[-3, 3, 6, 18, 26, 34, 42, 50, 58, 66, 74, 82] \times \sigma_{cont}$, where $\sigma_{cont} = 0.22$ mJy beam^{-1} in the third panel and 2 mJy beam^{-1} in the last panel (convolved to the same resolution as the CO). Synthesized beam sizes of the VLA and the ALMA data are shown as gray (ALMA) and yellow (VLA) filled ellipses in the lower left corners of the first and third panels, and are the same as in Figures 17 and 4. For the tapered ALMA data, the beam size is $0''31 \times 0''26$. Both [CII] and dust continuum emission are almost as extended as CO($J = 1 \rightarrow 0$). X-NE is detected in both CO($J = 1 \rightarrow 0$) and 635 μm continuum (and [CII] emission; see Figures 3 and 4).

et al. 2003). This (general) model is therefore parameterized by five free parameters: a characteristic dust temperature (T_d); emissivity index (β); power-law index (α); normalization factor (f_{norm}); and λ_0. We impose uniform priors such that $T_d > 1$ K, $\beta \in [0.1, 20.0]$, $\lambda_0 \in [1.0, 400.0]$ μm, and $\alpha \in [0.1, 20.0]$. We adopt the statistical means and 68th percentiles of the resulting posterior probability distributions as the "best-fit" parameters. For comparison with literature values, we also fit MBB+power-law models without the wavelength-dependent optical depth parameter (i.e., assuming optically thin dust emission). All the best-fit parameters are listed in Table 5. We note that the 160 μm photometry data is poorly fitted, which may suggest the presence of a warmer dust component in HXMM05. However, with the data at hand, this dust component cannot be constrained. Fitting models to photometry excluding the 160 μm data yields physical parameters that are consistent with those listed in Table 5 within the uncertainties.

4.1.2. *MAGPHYS model*

To determine the stellar mass of HXMM05, we fit models to its full SED, sampled by the FUV-to-radio wavelength photometry using the high-z extension of MAGPHYS (da Cunha et al. 2008, 2015). This code exploits a large library of optical and IR templates that are linked together physically through energy balance, such that the UV-to-optical starlight is absorbed by dust and re-radiated in the FIR. A detailed explanation of the MAGPHYS code and the model priors are given by da Cunha et al. (2015).

Following da Cunha et al. (2015), upper limits are taken into account by setting the input flux densities to zero and uncertainties to upper limits. The best-fit SED is shown in Figure 9 and the resulting best-fit parameters are listed in Table 6.

Since in the best-fit model, the *Herschel*/PACS 160 μm measurement forces the dust peak to shorter wavelengths and

Table 5
Dust properties of HXMM05 obtained from fitting single-temperature MBB models to its dust SED.

Parameter		General	Optically thin
T_d	(K)	64^{+5}_{-1}	49^{+20}_{-14}
β		$2.2^{+0.3}_{-0.3}$	$1.8^{+0.5}_{-0.5}$
α		$2.2^{+0.1}_{-0.2}$	$2.1^{+0.1}_{-0.2}$
λ_0 [a]	(μm)	170^{+20}_{-20}	—
f_{norm} [b]	(mJy)	81^{+6}_{-6}	67^{+16}_{-17}
L_{FIR} [c]	($10^{13} L_\odot$)	$2.4^{+0.2}_{-0.1}$	$2.2^{+3.1}_{-0.8}$
L_{IR} [d]	($10^{13} L_\odot$)	$4.6^{+0.2}_{-0.3}$	$4.5^{+3.0}_{-5.0}$
M_d [e]	($10^9 M_\odot$)	$1.4^{+0.3}_{-0.3}$	$4.3^{+0.8}_{-4.0}$

[a] Rest-frame wavelength where $\tau_\nu = 1$.
[b] Normalization factor/flux density at observed-frame 500 μm.
[c] Rest-frame $42.5 - 122.5$ μm luminosity.
[d] Rest-frame $8 - 1000$ μm luminosity.
[e] Derived assuming an absorption mass coefficient of $\kappa = 2.64$ m^2 kg^{-1} at $\lambda = 125.0$ μm (Dunne et al. 2003).

worsens the fit at long wavelengths (similar to the MBB fit), we re-model the SED excluding this outlier. The resulting best-fit parameters are listed in Table 6. The dust peak in this fit is in good agreement with the (sub-)mm and radio photometry. The best-fit parameters determined with and without the PACS 160 μm photometry are consistent within the uncertainties. We thus adopt the parameters from the latter fit (i.e., excluding the 160 μm outlier) in the following sections.

4.2. *Dynamical Modeling*

We fit dynamical models to the 1-kpc resolution [CII] data obtained with ALMA to study the gas dynamics of HXMM05 (more specifically, X-Main). The monotonic velocity gradient observed in [CII] suggests that HXMM05 is a rotating disk galaxy, an interpretation further supported by the analysis of §4.2.1 below.

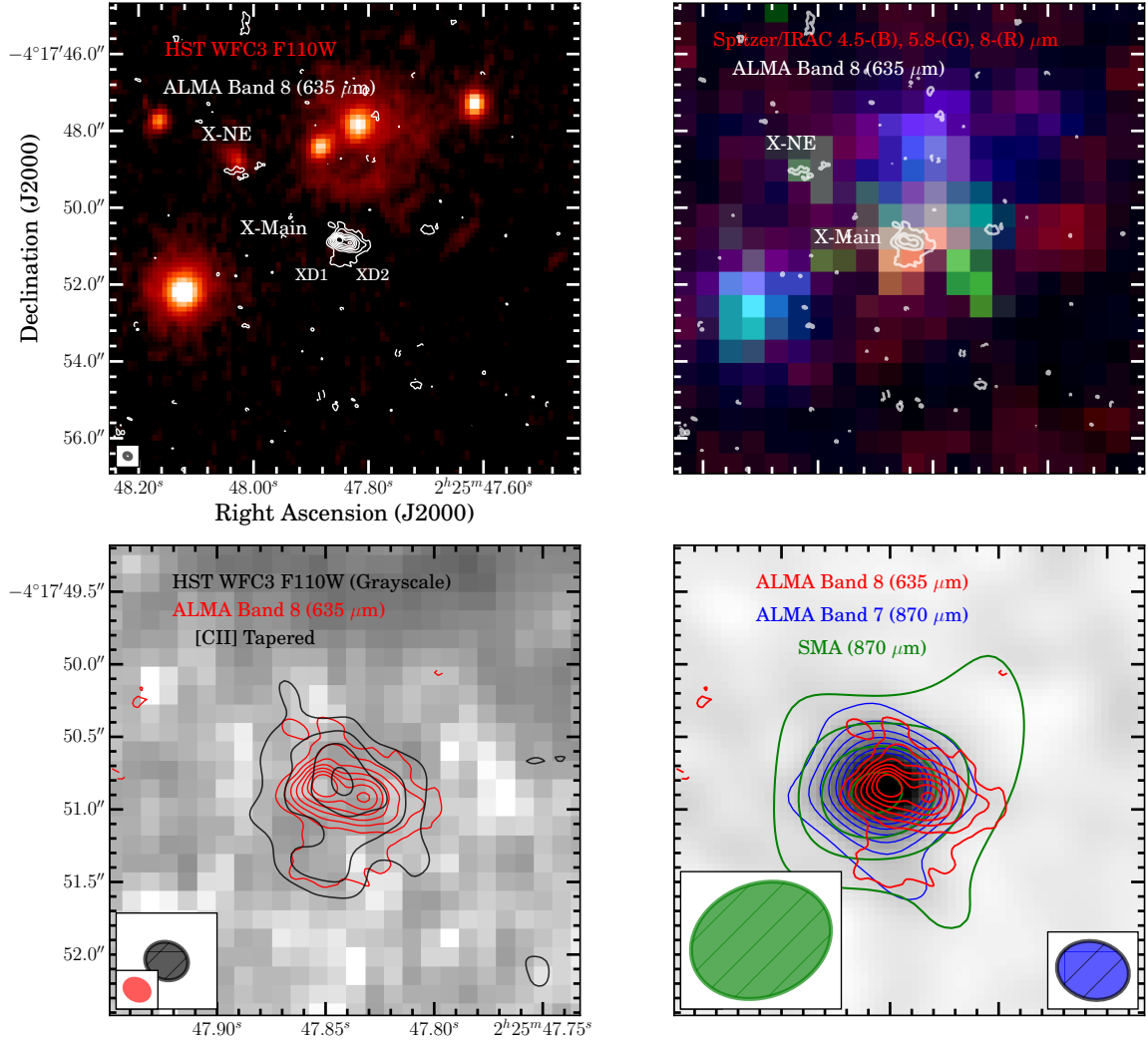Assuming that the disk is circular and infinitesimally thin,

Figure 8. ALMA 635 μm continuum emission (white contours) overlaid on an *HST* image (color-scale; top left; Calanog et al. 2014) and on a composite RGB image created from *Spitzer*/IRAC 4.5 (blue), 5.8 (green), and 8 μm (red) data (top right). Emission detected at 4.5 μm is dominated by foreground sources (see also Figure 19 in Appendix §C), but emission at 5.8 and 8 μm is dominated by HXMM05. In addition, X-NE is detected in the UV/optical/NIR wavebands and in the CO ($J = 1 \rightarrow 0$) and [CII] lines (see Figures 3 and 4). Bottom left: Contours of tapered [CII] (black) and full resolution continuum (red) emission overlaid on the same *HST* image as the top left panel (grayscale). Bottom right: ALMA 635 μm (red) and SMA 870 μm (green) continuum contours overlaid on the ALMA 870 μm image (blue contours and grayscale). Note the different angular scales shown for the two rows. Two distinct peaks seen at 635 μm are spatially offset from the [CII] emission. One dust peak is detected at 870 μm (XD1) and the other is SW of it (which we denote as XD2). Contours are shown in steps of $\pm 3n \times \sigma$, where n is an integer, $\sigma_{635} = 0.22$ mJy beam^{-1} for ALMA 635 μm, $\sigma_{870,\mathrm{ALMA}} = 0.28$ mJy beam^{-1} for ALMA 870 μm, $\sigma_{870,\mathrm{SMA}} = 0.92$ mJy beam^{-1} for SMA 870 μm, and $\sigma_{\mathrm{[CII]}} = 0.68$ Jy km s^{-1} for the tapered [CII] emission. Synthesized beams are color-coded by the contours shown in the lower corner of each panel: $0\rlap{.}''18 \times 0\rlap{.}''14$ (full resolution [CII]), $0\rlap{.}''31 \times 0\rlap{.}''26$ (tapered [CII]), $0\rlap{.}''99 \times 0\rlap{.}''78$ (SMA 870 μm), and $0\rlap{.}''5 \times 0\rlap{.}''4$ (ALMA 870 μm).

we use the kinematic major and minor axes to estimate the inclination angle, which yields $i = 46 \pm 8°$. This is slightly different from the value estimated using the morphological axes, which yields $i = 35 \pm 5°$, but the two are consistent within the error bars. We initialize the inclination angle in the following analyses based on these estimates.

4.2.1. *Harmonic Decomposition and Tilted-ring Model*

To assess whether the velocity field observed towards HXMM05 is consistent with its gas being distributed in a disk rather than effects caused by e.g., merging clumps, tidal debris, or inflows, we apply harmonic decomposition analysis (Schoenmakers et al. 1997). Briefly, this method describes higher order moments, K (e.g., LOS velocity) as a Fourier se-

ries:

$$K(\psi) = A_0 + A_1 \sin(\psi) + B_1 \cos(\psi) + \\ A_2 \sin(2\psi) + B_2 \cos(2\psi) + \cdots,$$

where ψ is the azimuthal angle measured from the major axis. The above can be recast into the following form:

$$K(r, \psi) = A_0(r) + \sum_m K_m(r) \cos\{m[\psi - \psi_m(r)]\}, \quad (2)$$

where the amplitude and phase of the m-th order term are defined as

$$K_m \equiv \sqrt{A_m^2 + B_m^2} \quad \text{and} \quad \psi_m \equiv \arctan \frac{A_m}{B_m}. \quad (3)$$

Table 6
Properties of HXMM05 from modeling its full SED with MAGPHYS.

	Parameter	All Photometry	Excluding $160\,\mu$m [a]
T_d	(K)	48^{+9}_{-1}	44^{+6}_{-5}
$L_{\rm IR}$ [b]	$(10^{13}\,L_\odot)$	$4.1^{+1.4}_{-0.4}$	$3.9^{+0.7}_{-0.4}$
SFR [c]	$(M_\odot\,{\rm yr}^{-1})$	3250^{+890}_{-420}	2900^{+750}_{-595}
M_*	$(10^{11}\,M_\odot)$	$7.2^{+9.0}_{-3.8}$	12^{+13}_{-7}
sSFR	$({\rm Gyr}^{-1})$	$4.7^{+4.7}_{-2.6}$	$2.4^{+4.3}_{-1.4}$
$M_{\rm d}$ [d]	$(10^9\,M_\odot)$	$3.0^{+0.7}_{-0.7}$	$3.4^{+0.4}_{-0.3}$

[a] The $160\,\mu$m photometry forces the dust peak to shorter wavelengths, such that the photometry data long-ward thereof are poorly fitted — motivating the choice of reporting both fits (see §4.1.2).
[b] Rest-frame $8-1000\,\mu$m luminosity.
[c] Assuming a Chabrier (2003) IMF.
[d] Derived by assuming the same absorption mass coefficient of $\kappa = 2.64\,{\rm m}^2\,{\rm kg}^{-1}$ at $\lambda = 125.0\,\mu$m as in the MBB models.
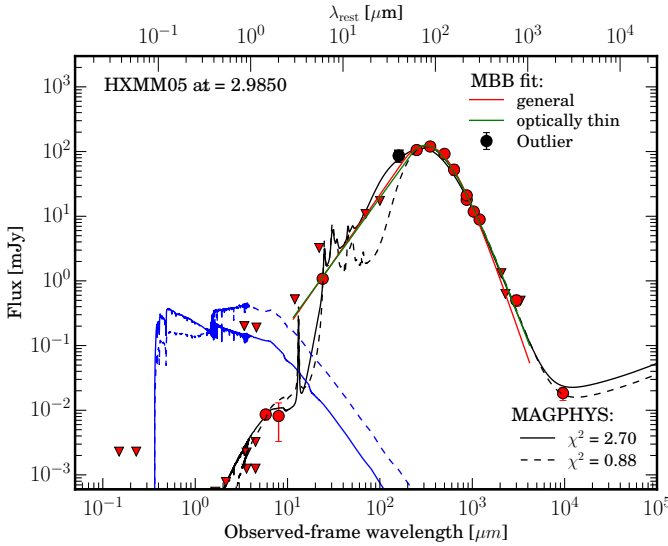
Figure 9. Best-fit MBB models (red and green solid lines) fitted to photometry covering $24\,\mu$m through 3 mm (error bars are also plotted, but since flux densities are shown on log-scale, they are not clearly visible). The red line shows the best-fit general MBB model and the green line shows the best-fit optically thin model. Solid black line shows the (attenuated) full SED obtained with MAGPHYS using photometry from FUV through 1 cm. Dashed black line shows the full SED fit excluding the $160\,\mu$m photometry (see text). Blue lines show the unattenuated stellar spectra.

Since the velocity field is expected to be dominated by the cosine term in the case of an ideal rotating disk; in this scenario, B_1 should dominate the harmonic terms, with higher order terms K_m measuring deviations from the ideal case. Following Krajnović et al. (2006), we compare the fifth-order amplitude term to the first-order cosine term (K_5/B_1) to quantify deviations in the [CII] velocity map of HXMM05 from a rotating disk, and thus, differentiate between a rotation-dominated disk and a dispersion-dominated merger. As shown in Figure 10, the higher order term is insignificant compared to B_1 across the majority of the disk, especially towards the center, where the data have higher S/N. We thus interpret HXMM05 to be a rotating disk for the remainder of this paper.
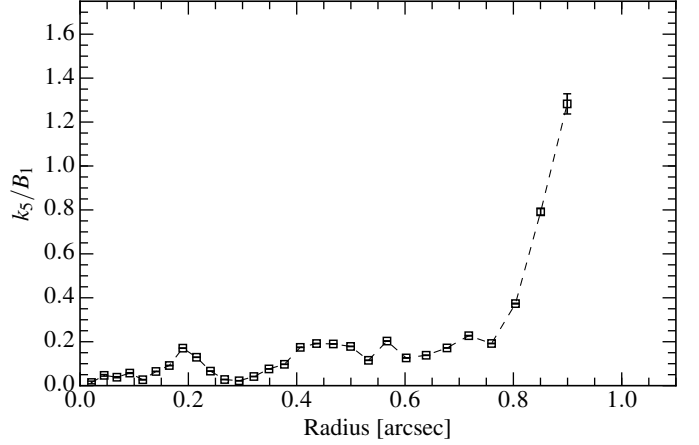
Figure 10. Ratio between the fifth- and first-order terms of the harmonic expansion of the [CII] velocity field (K_5/B_1) as a function of radius. The higher order term is insignificant compared to B_1 across nearly the entire disk, especially towards the center ($R = 0$), where the data have higher S/N.

Given the modest inclination of HXMM05, we fit tilted-ring models (Begeman 1989) to the observed velocity field using the task ROTCUR provided in the GIPSY software package to analyze the gas dynamics of HXMM05 due to bulk motions (i.e., driven by the gravitational potential). The tilted-ring model assumes that the gas is in a circular, rotating thin disk, and describes the disk using a series of concentric rings, where each ring can have an independent inclination angle (i), major axis PA, rotation velocity ($v_{\rm rot}$), and expansion velocity ($v_{\rm exp}$). The rotation velocity is related to the projected LOS velocity via

$$v_{\rm LOS} = v_{\rm sys} + v_{\rm rot}\cos\left(\psi\right)\sin\left(i\right) + v_{\rm exp}\sin\left(\psi\right)\sin\left(i\right). \quad (4)$$

Here, we assume that the observed LOS velocity is due entirely to disk rotation and ignore any radial motions (e.g., due to inflow/outflow) by setting the expansion velocity to $0\,{\rm km\,s}^{-1}$ (i.e., the higher order K_m terms). We fit the model iteratively with different sets of parameters held fixed, while varying others freely. We adopted this approach because each ring would have six free parameters otherwise ($x_{\rm cen}$, $y_{\rm cen}$, $v_{\rm sys}$, i, PA, $v_{\rm rot}$), which our data do not allow us to fix simultaneously, especially because $v_{\rm rot}$ and i are highly degenerate. Without doing so, models struggle to converge to a solution[19]. The fact that this approach is also adopted in modeling the kinematics of local galaxies, where the data obtained have much higher S/N and spatial resolution, shows that our data do not offer such constraining power (e.g., Swaters et al. 2009; van Eymeren et al. 2009; Elson 2014; Hallenbeck et al. 2014; Di Teodoro & Fraternali 2015; Jovanović 2017). This approach is also adopted in fitting low-S/N and coarser spatial resolution data obtained at high redshift (see e.g., Shapiro et al. 2008). Here, we minimize the set of freely varying parameters via least-squares fitting. Except in the last iteration, the width of each ring is set to the beam size. In the first iteration, the dynamical center ($x_{\rm cen}$, $y_{\rm cen}$) and systemic velocity

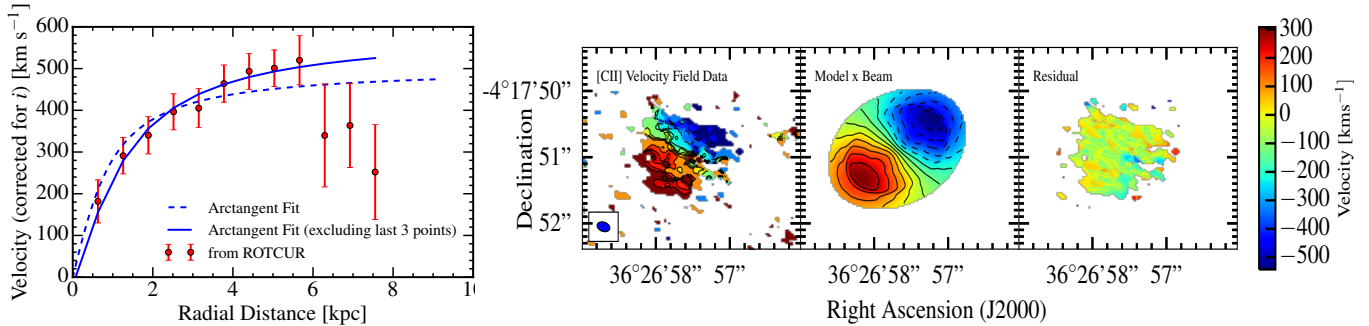[19] We have tested this by allowing i and PA also to vary across rings.

Figure 11. Left panel: Rotation curve of HXMM05 based on a tilted-ring model and an extrapolation using an arctangent function. The *y*-axis shows the rotation velocity after correcting for an inclination angle of $i = 41.3°$. Beyond a radius of $R = 6$ kpc, the rotation velocity appears to drop off, but this decrease is most likely related to the limited S/N in the reddest velocity channels (see Figure 16 in Appendix §A). Right panel from left to right: Velocity fields seen in the data, best-fit model, and residual. Uniform velocities varying between $v \in [0, 100]$ km s^{-1} are seen across the residual map.

($v_{\rm sys}$) vary freely, whereas the inclination angle is fixed to the average value found from the kinematic and morphological axes, and the PA is fixed to the photometric/morphological PA. We then constrain *i*, PA, and $v_{\rm rot}$ while fixing $x_{\rm cen}, y_{\rm cen}$, and $v_{\rm sys}$ to their weighted-average values found in the previous iteration. To better determine the inclination angle, we further fix the PA and fit for *i* and $v_{\rm rot}$ only. In the final run, we fix all parameters to the weighted averages found in the previous iterations and only fit for $v_{\rm rot}$, and the width of each ring is set to half the beam size to sample the rotation curve. From the model, we find a best-fit PA of $133.6° \pm 0.6°$ (east of north). and an inclination of $i = 41.3° \pm 3.9°$.

After this determination, the best-fit parameters are used to form the model velocity field using the VELFI task. A residual image (Figure 11) is obtained by subtracting the model (after convolving with the beam) from the data. The residual is largely uniform across the entire disk, with velocities varying by less than 100 km s^{-1}, consistent with the velocity dispersion map observed in Figure 5. The relatively low residuals indicate that the best-fit model is a reasonable description of the observed velocity field, and that non-circular motions (e.g., streaming motions along unseen spiral arms or bars, or large-scale tidal torquing from galaxy interactions) are unlikely to be detected in the kpc-scale resolution data. We note that beam smearing means that velocity information within the inner kpc region will be largely lost in the data.

We fit an arctangent model (e.g., Courteau 1997) to the ROTCUR rotation curve (RC). The model is parameterized as:

$$V_{\rm rot} = V_0 + \frac{2}{\pi} V_a \arctan\left(\frac{R}{R_t}\right), \quad (5)$$

where $V_{\rm rot}$ is the rotation velocity found with ROTCUR, V_0 is the systemic velocity, V_a is the asymptotic velocity, and R_t is the "turnover" radius at which the rising part of the rotation curve begins to flatten. We perform non-linear least-squares fitting using the Levenberg-Marquardt algorithm to find the best-fit parameters. We limit the turnover radius to $0 < R_t < 25$ kpc in order to keep this parameter within a physically meaningful range. Using this model, we find $V_a = 503 \pm 83$ km s^{-1}, $R_t = 0.8 \pm 0.3$ kpc,

and $V_0 = 0 \pm 28$ km s^{-1} (relative to the systemic redshift). We thus find an inclination-corrected rotation velocity of $v_{\rm rot} = 474 \pm 78$ km s^{-1} at a spatial offset of 8.8 kpc (the extent of the ground state CO line emission; Table 3). We note that the model underestimates the velocities at $R \gtrsim 4$ kpc because of the outermost three data points at >6 kpc, which deviate from the trend of increasing velocity with radius. Such a trend — a declining rotation curve with increasing galactocentric radius — has been reported in some studies of high-*z* galaxies (e.g., Genzel et al. 2017; Lang et al. 2017, cf. e.g., Tiley et al. 2018). In our data, this trend is likely an artifact due to the limited S/N at those PV-positions (i.e., low number of pixels fitted; see Figures 6 and 16 in Appendix §A). In other words, the decreasing velocities seen at increasing radius in our target could easily be mimicked by a lack of sensitivity to low surface brightness emission in the outer regions. If we instead fit the arctangent model excluding these three data points, we find an inclination-corrected rotation velocity of $v_{\rm rot} = 537 \pm 83$ km s^{-1} at 8.8 kpc and an asymptotic velocity of $V_a = 617 \pm 97$ km s^{-1}. Both models are consistent within the uncertainties.

Rotation curves from both arctangent models do not reach the terminal velocity[20] (i.e., the flat part of the rotation curve). Therefore, the rotation velocities inferred here may be lower limits only. On the other hand, part of the rotation curve that is flattening is clearly detected in the PV-diagram (Figure 6). This discrepancy is related to the fact that fitting models to velocity fields can underestimate true rotation velocities,[21] and that the decreasing velocities seen in the outermost three data points of the rotation curve are of limited S/N. This flattening part of the rotation curve detected in HXMM05 is likely to be mainly driven by the dynamics of the parent dark matter halo, as in nearby galaxies; we see no evidence indicating that HXMM05 is dominated by baryons from the data at

---

[20] Terminal velocity is not the same as asymptotic velocity, which the arctangent model *does* constrain.

[21] This underestimation occurs because velocity fields are intensity-weighted and the tilted-ring model assumes that all the gas in a ring is at a unique position along the LOS; however, gas emission from other velocities along the LOS is blended within the beam. Thus, the lower the resolution, the more likely the true velocities are underestimated by fitting models to the velocity fields.

hand. Adopting the inclination-corrected V_a as the maximum rotation velocity, we find that HXMM05 is consistent with the gas Tully-Fisher relation found for nearby galaxies, given its gas mass (see Table 7; McGaugh & Schombert 2015).

4.2.2. *Envelope-Tracing Method*

As an alternative approach to estimate the rotation velocity of HXMM05, we also use the envelope-tracing (ET) method, where we fit models to the PV diagram extracted along the kinematic major axis (Figure 6; see review by Sofue & Rubin 2001). The ET method attempts to trace out the material that has the maximum tangential motion along each LOS (see Figure 5 of Chemin et al. 2009 for a schematic depiction of this geometric effect).

We fit a third order (h_3) Gauss-Hermite polynomial to a (Hanning-smoothed) spectrum extracted at each position along the PV cut (Figure 6) to account for any asymmetries in the spectra. The rotation curve (traced by the "envelope") is derived from the terminal velocity ($v_t^{\rm obs}$) at which 8% of the total flux under the fitted curve is outside $v_t^{\rm obs}$. In essence, this approach traces the isophotes at each position along the kinematic major axis.

The innermost 1.5 kpc region of the PV diagram is steeply rising (Figure 6), which is due in part to the facts that the velocity gradient in this region is changing rapidly from positive to negative, and that contributions from multiple radii overlap in the inner roughly 1 kpc (which remains unresolved at the ~ 1.2 kpc resolution of the data). Structures within the "envelope" modulo inclination and beam smearing effects may result from the presence of spiral- or ring-like structures, or a clumpy gas distribution in HXMM05.

Based on the terminal velocity, we derive the rotation velocity of HXMM05 using the following equation:

$$v_{\rm rot} = (v_t^{\rm obs} - v_{\rm sys})/\sin(i) - \sqrt{(\sigma_{\rm PSF}^2 + \sigma_{\rm ISM}^2)}, \qquad (6)$$

where $v_{\rm sys}$ is the systemic velocity determined from fitting a double-Gaussian to the [CII] spectrum (Figure 1), i is the inclination angle from ROTCUR, $\sigma_{\rm PSF}$ is the spectral resolution, and $\sigma_{\rm ISM}$ is the velocity dispersion of the gas (see e.g., Vollmer et al. 2016 and Sofue 2017). Here, we adopt the observed velocity dispersion of $\sigma_v = 75$ km s^{-1} as the subtracted term. We then re-sample the rotation profile every half beam (instead of every pixel) and show the output rotation curve in Figure 6. We find an inclination-corrected rotation velocity of $v_{\rm rot} = 616 \pm 100$ km s^{-1} at the last measured radius of the rotation curve ($R = 8.0$ kpc), which is consistent with the rotation velocity of $v_{\rm rot} = 537 \pm 83$ km s^{-1} derived from the arctangent model within the uncertainties.

4.3. *PDR modeling*

Photo-dissociation regions (PDRs) are the warm and dense surfaces of molecular clouds exposed to FUV photons with energies $6 < h\nu < 13.6$ eV escaping from HII regions. In PDRs, gas temperatures and densities are typi-

cally $T = 100 - 500$ K and $n = 10^{2-5}$ cm^{-3}. Since the [CII] 158 μm line is the primary coolant in PDR conditions satisfying $n \lesssim 10^3$ cm^{-3} and $T \lesssim 100$ K, [CII] and other ISM lines near or in PDRs are sensitive probes of the physical conditions of the PDR gas and the intensity of the ambient interstellar radiation field (G_0; conventionally expressed in units of 1.6×10^{-3} erg cm^{-2} s^{-1}, the Habing flux; e.g., Hollenbach & Tielens 1999). Using the [CII] and CO line luminosities and the PDR model grids from Tielens & Hollenbach (1985) and Kaufman et al. (1999, 2006)[22] , we constrain the globally-averaged G_0, hydrogen density (n), and surface temperature for the PDRs in HXMM05[24]. We adopt CO grids from an updated version of the code (Hollenbach et al. 2012; M. Wolfire 2017, private communication) that is merged with the MEUDON code (Le Petit et al. 2006) for a more detailed treatment of H_2 chemistry and thermal balance.

The observed line ratios are shown in Figure 12 as functions of G_0 and n. Since a fraction of the [CII] emission in the ISM arises outside of PDRs, and we lack other diagnostic lines to determine this fraction in HXMM05, we adopt a canonical value of 30% to account for this non-PDR contribution (Carral et al. 1994; Colbert et al. 1999; Malhotra et al. 2001; Oberst et al. 2006; see also Pavesi et al. 2016, 2018; Zhang et al. 2018b). CO line emission is typically optically thick (especially the low-J lines), and so we multiply their line intensities by a factor of 2 to account for the emission on the other side of the surface. Corrections are incorporated into the line ratios as uncertainties (filled regions in Figure 12). The best-fit model is determined based on the global minimum χ^2, corresponding to log $n = 4.5$ cm^{-3} and log $G_0 = 2.25$. Based on the χ^2 surface, the uncertainties in both n and G_0 are approximately an order of magnitude. As discussed by Röllig et al. (2007), physical parameters inferred from any PDR models should not be taken too literally, since they are subject to differences depending on the assumptions adopted and the implementation of microphysics in the code. Nevertheless, we use the best-fit parameters as simple approximations to compare HXMM05 with other galaxies.

The lower G_0 solution ($G_0 < 1$) implied by the mid-J CO and [CII]-to-FIR ($L_{\rm [CII]}/L_{\rm FIR}$) luminosity ratios disagrees with that implied by the CO ($10 \rightarrow 9$)-to-($1 \rightarrow 0$) and [CII]-to-CO ($J = 1 \rightarrow 0$) luminosity ratios. We reject this low G_0 solution since it would require a physically enormous emitting region to account for the observed high $L_{\rm FIR}$ in HXMM05 ($G_0 \propto L_{\rm FIR}/D^2$; Wolfire et al. 1990). Assuming the values for M82 ($D \simeq 300$ pc, $G_0 \simeq 1000$, $L_{\rm FIR} \simeq 2.8 \times 10^{10} L_\odot$), the solution with $G_0 \simeq 0.2$ would require an emitting region $D = 600$ kpc in size, contrary to what is observed. On the other hand, the best-fit $G_0 \sim 200$ corresponds to an emit-

---

[22] Available through the PDR Toolbox[23] described by Pound & Wolfire (2008) and Wolfire et al. (2010)

[24] While it is physically unrealistic to model an entire galaxy as a single PDR, we infer the G_0 and n values of HXMM05 in a globally-averaged sense to facilitate comparison with other studies in the literature.

ting region of $D \simeq 20\,\mathrm{kpc}$, which is more consistent with the sizes observed in [CII] and CO$(J=1\rightarrow 0)$ line emission (Table 3). The FUV radiation field intensity of HXMM05 is thus stronger than the local Galactic interstellar radiation field intensity by a factor of around 200, comparable to the values found in nearby normal star-forming galaxies and those found in some other DSFGs (e.g., Malhotra et al. 2001; Wardlow et al. 2017). The best-fit G_0 and n together suggest a surface temperature of $T_{\mathrm{surf}} = 290\,\mathrm{K}$ for the PDR. We approximate the PDR pressure using $P \propto nT$, yielding $P/k_B = 9.0 \times 10^6\,\mathrm{cm}^{-3}\,\mathrm{K}$. We note that an offset is found between the CO$(J=10\rightarrow 9)$/CO$(J=1\rightarrow 0)$ line and the other luminosity ratios in the $\log n - \log G_0$ plane. This offset likely results from the fact that CO$(J=10\rightarrow 9)$ emission preferentially traces a more highly-excited phase of the ISM than the other lines (e.g., due to mechanical heating or X-ray heating; see also §5.6). However, with the data at hand, the presence and properties of an X-ray dominated region (and/or a second PDR component, and/or shock excitation) are unconstrained and indistinguishable from a simple single PDR.

The PDR properties thus suggest that the high far-IR luminosity of HXMM05 ($> 10^{13}\,L_\odot$) may result from extended star formation, with only a modest FUV radiation field intensity. This is in stark contrast with the compact starbursts seen in the cores of many nearby ULIRGs (less than a few hundred parsecs), which are found to have stronger FUV radiation fields compared to HXMM05 (e.g., Stacey et al. 2010). The inferred PDR conditions also suggest that HXMM05 is unlikely to host an AGN or a powerful quasar, consistent with §5.1.
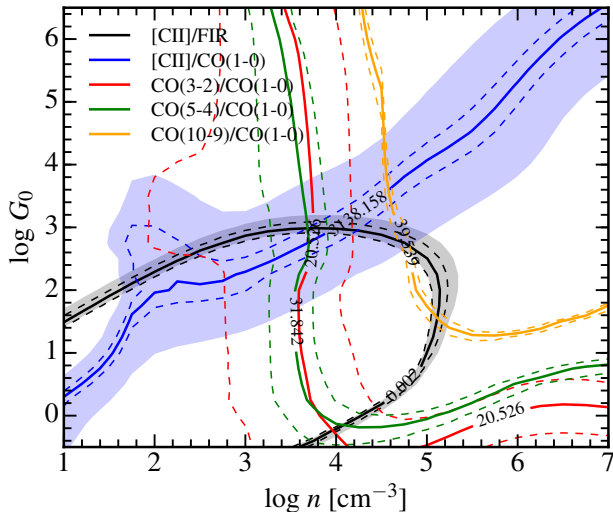
Figure 12. Ratios of CO, [CII], and far-IR luminosities (solid) as functions of G_0 and n. Model grids are adopted from PDR Toolkit, except for the CO grids (see text). Dashed lines show the uncertainties associated with these ratios. Filled regions show larger uncertainties, after including the corrections for the non-PDR fraction of [CII] emission (30%) and the factor of 2 in CO due to optically thick CO emission (see text).

5. DISCUSSION

Table 7
Physical properties of HXMM05 obtained from dynamical, SED, and PDR modeling.

Parameter	Unit	Value
$r_{3,1}$ [a]		0.76 ± 0.28
$r_{5,1}$ [a]		0.26 ± 0.10
$r_{10,3}$ [a]		0.04 ± 0.01
$r_{10,1}$ [a]		0.03 ± 0.01
i	deg	41.3 ± 3.9
CO$(J=1\rightarrow 0)$ extent	kpc	8.8 ± 2.6
Rotation curve radius	kpc	8.0
Maximum v_{rot} [b]	km s^{-1}	616 ± 100
$M_{\mathrm{dyn}}(R < 8.0\,\mathrm{kpc})$ [b]	$10^{11}\,M_\odot$	7.7 ± 3.1
Observed $\sigma_{\mathrm{[CII]}}$	km s^{-1}	100 ± 25
$L_{\mathrm{[CII]}}$	$10^{10}\,L_\odot$	4.3 ± 0.5
L_{CO}	$10^7\,L_\odot$	1.3 ± 0.4
$M_{\mathrm{gas}}^{\mathrm{total}}$	$10^{11}\,M_\odot$	2.1 ± 0.7
$M_{\mathrm{gas}}^{\mathrm{X-Main}}$	$10^{11}\,M_\odot$	1.7 ± 0.4
$M_{\mathrm{gas}}^{\mathrm{X-NE}}$	$10^{10}\,M_\odot$	6.5 ± 1.6
L_{IR} [c]	$10^{13}\,L_\odot$	$3.9^{+0.7}_{-0.4}$
SFR [d]	$M_\odot$ yr^{-1}	2900^{+750}_{-595}
T_d	K	44^{+6}_{-5}
M_d [e]	$10^9\,M_\odot$	2.9 ± 1.5
M_*	$10^{12}\,M_\odot$	$1.2^{+1.3}_{-0.7}$
GDR [e]		$50 - 145$
$f_{\mathrm{gas}}^{\mathrm{dyn}}$ [f]	%	33 ± 15
$f_{\mathrm{gas}}^{\mathrm{dyn,iso}}$ [g]	%	5.3 ± 2.4
M_{gas}/M_*		$0.2^{+0.2}_{-0.1}$
$M_{\mathrm{gas}}/(M_{\mathrm{gas}} + M_*)$		0.2 ± 0.2
τ_{depl}	Myr	72 ± 27
SFE [h]	Gyr^{-1}	13 ± 4
$L_{\mathrm{[CII]}}/L_{\mathrm{FIR}}$ [i]	%	0.20 ± 0.03
$L_{\mathrm{[CII]}}/L_{\mathrm{CO}}$ [i]		3300 ± 1000
$L_{\mathrm{CO}}/L_{\mathrm{FIR}}$ [i]	10^{-7}	5.5 ± 1.9
$12 + \log(\mathrm{O/H})$ [j]		9.1
$\alpha_{\mathrm{CO,Z}}$ [k]	$M_\odot$ (K km pc^2)$^{-1}$	$1.4 - 1.9$
$\Sigma_{\mathrm{SFR}}^{\mathrm{XD1}}$	$M_\odot$ kpc^{-2} yr^{-1}	210
$\Sigma_{\mathrm{SFR}}^{\mathrm{XD2}}$	$M_\odot$ kpc^{-2} yr^{-1}	120
Σ_{SFR}	$M_\odot$ kpc^{-2} yr^{-1}	10
Σ_{mol}	$M_\odot$ pc^{-2}	590 ± 410

Note. — Any quantities in this table relating to the gas mass (and throughout this paper) are derived from CO$(J=1\rightarrow 0)$ emission, assuming $\alpha_{\mathrm{CO}} = 0.8\,M_\odot$ (K km pc^2)$^{-1}$ and using the total molecular gas mass (i.e., both X-Main and the NE component combined) unless otherwise specified.
[a] Brightness temperature ratio between two CO rotational transitions: r.
[b] From PV fitting, see §4.2.2.
[c] From SED modeling excluding the photometry obtained with *Herschel*/PACS at 160 μm and *Spitzer*/MIPS 24 μm (see §4.1.2). Integrated over rest-frame $8 - 1000\,\mu$m luminosity.
[d] Averaged over the last 100 Myr and assuming a Chabrier (2003) IMF.
[e] Dust masses derived from MBB and full SED modeling lie in the range of $M_d = (1.44 - 4.27) \times 10^9\,M_\odot$, which is within the uncertainties due to intrinsic uncertainties in κ_ν (see §4.1). Here we quote the average dust mass as the centroid value and use the extreme values as the uncertainty.
[f] M_{dyn} determined from dynamical modeling (§5.4).
[g] Determined using $M_{\mathrm{dyn}} = 2.8 \times 10^5\,\Delta v_{\mathrm{FWHM}}^2\,R_{\mathrm{FWHM}} = (3.89 \pm 1.09) \times 10^{12}\,M_\odot$ to compare HXMM05 with other high-z galaxies reported in the literature.
[h] SFE $\equiv L_{\mathrm{FIR}}/M_{\mathrm{gas}}$, where $L_{\mathrm{FIR}} = 2.39^{+0.16}_{-0.14} \times 10^{13}\,L_\odot$.
[i] Observed quantities. No corrections applied (see §4.3).
[j] Based on the FMR derived by Mannucci et al. (2010). On the PP04 scale, the metallicity of HXMM05 is $12 + \log(\mathrm{O/H})_{\mathrm{PP04}} = 8.74$.
[k] Based on the α_{CO}-metallicity relation derived by Leroy et al. (2011) and Genzel et al. (2012) (see §5.2.2).

Since X-Main and X-NE remain spatially unresolved from each other in the IR photometry and most of the spectral line data (except in CO $J = 1 \rightarrow 0$ and [CII] emission), we discuss the properties of HXMM05 as a combined system in the following sections.

5.1. *No Evidence of an AGN in HXMM05*

Given the upper limits imposed on the X-ray luminosity of HXMM05, we find no evidence for the presence of a powerful AGN, but we *cannot* rule out the possibility of a heavily dust-obscured AGN in HXMM05 or a Seyfert galaxy nucleus with modest X-ray emission. To assess the reliability of the stellar mass derived from SED fitting, we examine if the mid-IR spectral slope of HXMM05 ($S_\nu \propto \nu^\alpha$) may be consistent with a low X-ray luminosity AGN (see e.g., Stern et al. 2005; Donley et al. 2007). We fit a power-law to the IRAC 5.8- and MIPS 24-μm photometry, which correspond to rest-frame $1.5 - 6.0\,\mu$m. We find a spectral index $\alpha_{1.5-6,\mathrm{rest}} = 1.46 \pm 0.58$, which is much flatter than those observed in AGN host galaxies[25] (Stern et al. 2005; Donley et al. 2007, 2008), suggesting that the NIR emission in HXMM05 may be dominated by stellar emission. Thus, we assume in the following that all the NIR emission detected in the IRAC channels 3 and 4 bands arises solely from the starlight in HXMM05. That is, the accuracy of the stellar mass estimated is dominated by the uncertainty on the IMF adopted (see e.g., Zhang et al. 2018a). If HXMM05 were to host an AGN, however, its stellar mass and SFR would be overestimated.

5.2. *ISM Properties*

5.2.1. *Stellar Mass and Specific Star Formation Rate*

We find an unusually high stellar mass of $10^{12}\,M_\odot$ for HXMM05 from SED modeling. The stellar mass estimate relies heavily on IRAC channels 3 and 4 (i.e., rest-frame 1.4 and 2.0 μm) photometry. Previous studies have shown that rest-frame K-band (2.2 μm) photometry appears to be a reliable proxy[26] for the stellar mass of galaxies, since photometry in this band is relatively insensitive to the past star-formation histories of galaxies (e.g., Kauffmann & Charlot 1998; Lacey et al. 2008; cf. Kannappan & Gawiser 2007), and because NIR emission is less affected by dust extinction compared to optical light. In particular, the difference in the K-band luminosity between initial burst and constant star formation models is less than a factor of 3 (e.g., Pérez-González et al. 2008). The main systematic uncertainties associated with M_* are therefore the star-formation histories assumed, the IMF and stellar population synthesis model adopted, and the fact

that differential dust extinction is not captured in simple energy balance models (e.g., MAGPHYS)[27]. Nevertheless, the stellar masses inferred from MAGPHYS are found to match the true masses of mock galaxies in simulations fairly well (e.g., Michałowski et al. 2014; Hayward & Smith 2015; Smith & Hayward 2015), unless the dust attenuation in HXMM05 is underestimated by MAGPHYS. Taken at face value[28], the high stellar mass suggests that a substantial fraction of stars may have already formed in some massive galaxies by $z = 3$ (approximately 2 Gyr after the Big Bang).

The relatively tight "correlation" found between SFR and M_* for star-forming galaxies at low- and high-z suggests that the majority of galaxies are forming stars over a long duty cycle in a secular mode (e.g., Rodighiero et al. 2011; Lehnert et al. 2015). The specific SFR of sSFR $= 2.37^{+4.31}_{-1.43}\,\mathrm{Gyr}^{-1}$ of HXMM05 is consistent with the star-forming "main-sequence" (SFMS) within the scatter of the MS relations derived by Tacconi et al. (2013), Lilly et al. (2013), Speagle et al. (2014), and Schreiber et al. (2015), if we extrapolate them to higher masses and include the uncertainties associated with the SFR and stellar mass inferred for HXMM05. One possible caveat is the applicability of the SFMS relation, and whether our current knowledge of the MS is meaningful at high stellar mass ($10^{12}\,M_\odot$). In this paper, we only consider HXMM05 as a MS galaxy for the sake of comparing its ISM properties with other high-z MS and starburst systems.

5.2.2. *Gas Mass, Gas-to-Dust Ratio, and Metallicity*

Using the CO ($J = 1 \rightarrow 0$) line intensities (Table 3) and assuming a CO luminosity-to-H_2 mass conversion factor of $\alpha_{\mathrm{CO}} = 0.8\,M_\odot\,(\mathrm{K\ km\ pc}^2)^{-1}$ (e.g., Downes & Solomon 1998), we derive molecular gas masses of $M_{\mathrm{gas}}^{\mathrm{X-Main}} = (1.68 \pm 0.43) \times 10^{11}\,M_\odot$ for X-Main, $M_{\mathrm{gas}}^{\mathrm{NE}} = (6.52 \pm 1.63) \times 10^{10}\,M_\odot$ for X-NE, and $M_{\mathrm{gas}}^{\mathrm{total}} = (2.48 \pm 0.65) \times 10^{11}\,M_\odot$ for the entire system (Figure 2). Using the molecular gas mass of the system, we find a gas-to-dust mass ratio of GDR $(\alpha_{\mathrm{CO}}/0.8)^{-1} = 50 - 145$, which is consistent with those measured in the Milky Way, local spiral galaxies, ULIRGs, and DSFGs (Draine & Li 2007; Wilson et al. 2008; Combes et al. 2013; Bothwell et al. 2013).

Based on the fundamental metallicity relation (FMR) determined by Mannucci et al. (2010), we infer a gas-phase metallicity of $Z = 12 + \log(\mathrm{O/H}) = 9.07$ for HXMM05[29], which is comparable to the that of the $z = 4$ SMG GN20 (Magdis et al. 2011). We express the metallicity on the Pettini & Pagel (2004; PP04) scale using the calibration proposed by Kew-

---

[25] Spectral indices reported in the literature are based on photometry taken at $3.6 - 8.0\,\mu$m, which correspond to the closest wavelength range used here for HXMM05 in the rest-frame.

[26] Since the dust optical depth of HXMM05 at rest-frame 158 μm is $\tau_\nu \sim 1$, its K-band emission could be highly attenuated, unless most of the starlight is less attenuated than the dust (e.g., if the latter is dominated by compact star-forming knots and the former is much more extended), which remains possible given its dust morphology, gas excitation, and G_0.

[27] Alternatively, hot dust emission due to a deeply buried AGN could contribute to the observed IR luminosity, and thus lead to an overestimate of M_* (but see Michałowski et al. 2014, who find insignificant effects of AGN on the SED-derived M_*).

[28] Note, however, that even assuming no AGN is present in HXMM05, the M_* estimate is accurate to only $\lesssim 0.5$ dex (see also Michałowski et al. 2014) on top of the large statistical error bars reported in Table 6.

[29] This assumes that the FMR relation holds up to $z = 3$ and a stellar mass of $10^{12}\,M_\odot$ (see e.g., Steidel et al. 2014).

ley & Dopita (2002) and Kewley & Ellison (2008), yielding $Z_{PP04} = 8.74$. The range of GDR derived for HXMM05 is consistent with the best-fit $GDR - Z_{PP04}$ relation presented by Magdis et al. (2011), which was determined for a sample of local galaxies studied by Leroy et al. (2011). If the CO-to-H_2 conversion factor were $\alpha_{CO} > 0.8 \, M_\odot$ (K km pc^2)$^{-1}$, then HXMM05 would lie above this relation. By applying the $\alpha_{CO} - Z$ relations found by Leroy et al. (2011) and Genzel et al. (2012), we find a range of α_{CO} of $1.4 - 1.9 \, M_\odot$ (K km pc^2)$^{-1}$, which would increase the molecular gas mass by a factor of $1.7 - 2.4$ compared to the value assumed here.

5.2.3. *Dust, Gas, and Stellar Mass Ratios*

The dust-to-stellar mass ratio (DSR) measures the amount of dust per unit stellar mass that survives all dust destruction processes in a galaxy (e.g., type II SN explosions). The DSR of HXMM05 is $2.3^{+2.7}_{-1.8} \times 10^{-3}$, which is within the range measured in local star-forming galaxies and ULIRGs, but is among the lowest measured in intermediate-z ULIRGs and quasars (e.g., Dunne et al. 2011; Combes et al. 2013; Leung et al. 2017). This ratio is also lower than those measured in DSFGs at similar redshifts (e.g., Magdis et al. 2011; Calura et al. 2017).

The molecular gas-to-stellar mass ratio of HXMM05 is $M_{gas}/M_* = 0.2^{+0.2}_{-0.1}$, which is higher than those observed in local SFGs and early-type galaxies (e.g., Leroy et al. 2008; Saintonge et al. 2011; Young et al. 2014). Previous studies report a positive evolution in this ratio with redshift (e.g., Tacconi et al. 2010; Davé et al. 2012). The M_{gas}/M_* ratio of HXMM05 is lower than those typically measured in other high-z SFGs and DSFGs at $z > 1.2$, and is the lowest[30] found among massive galaxies at $z \simeq 3$ to date (Leroy et al. 2008; Tacconi et al. 2010; Daddi et al. 2010; Geach et al. 2011; Decarli et al. 2016).

The low DSR and gas-to-stellar ratio of HXMM05 may indicate that it is a relatively evolved system, in which a large fraction of its gas has been converted into stars and a large fraction of dust has been locked up in stars. That said, as discussed in §5.1 and §5.2.1, it is possible that the stellar mass maybe overestimated.

5.3. *Star Formation Efficiency and Gas Depletion Timescale*

To first order, the star formation efficiency (SFE) measures the star formation rate per unit mass of molecular gas available in a galaxy. The SFE of HXMM05 is $L_{FIR}/L'_{CO(1-0)}$ $= 91 \pm 25 \, L_\odot$ (K km s^{-1} pc^2)$^{-1}$ (or 13 ± 4 Gyr^{-1}), which is slightly higher than but consistent with the range found in nearby active star-forming spiral galaxies ($z < 0.1$; Gao & Solomon 2004; Solomon & Vanden Bout 2005; Stevens

et al. 2005; Leroy et al. 2008; Wilson et al. 2009; Leroy et al. 2013) and high-z massive disk-like galaxies (Daddi et al. 2008, 2010; Aravena et al. 2014). Assuming that the star formation in HXMM05 continues at its current rate without gas replenishment, the gas will be depleted in $\tau_{depl} = 72 \pm 27$ Myr[31], comparable to the depletion times in starburst systems. HXMM05 thus lies between SFMS and starburst galaxies in the so-called "transition region" on the integrated version of the "star-formation law" (i.e., $L_{FIR} - L'_{CO(1-0)}$ relation; Daddi et al. 2010; Magdis et al. 2012; Sargent et al. 2014). We conclude that the gas depletion timescale in HXMM05 is short compared to those of SFMS galaxies at high redshift.

5.4. *Dynamical Mass*

The rotation curve of a galaxy reflects its dynamics due to the total (i.e., baryonic and dark matter) enclosed mass. We estimate the total dynamical mass enclosed within 8 kpc using $M_{dyn} = v_{rot}^2 \, R/G$. We find an inclination-corrected dynamical mass of $M_{dyn} = (7.7 \pm 3.1) \times 10^{11} \, M_\odot$. Taken at face value[32], we find a molecular gas mass fraction of $f_{gas}^{dyn} = M_{mol}/M_{dyn} = 18 \pm 8\%$ using the gas mass of the main component of HXMM05 only (M_{gas}^{X-Main}) and $33 \pm 15\%$ using the total molecular gas mass of the system (M_{gas}^{total}). The dynamical mass is consistent with the stellar mass within the considerable uncertainties.

Since the dynamical masses derived for most other high-z galaxies in the literature are based on marginally resolved or unresolved observations, we also estimate the dynamical mass of HXMM05 using the isotropic estimator $M_{dyn}^{iso} = 2.8 \times 10^5 \, \Delta v_{FWHM}^2 \, R_{FWHM}$ (e.g., Engel et al. 2010), where Δv_{FWHM} is the CO $(J = 1 \rightarrow 0)$ line FWHM measured by fitting a single-Gaussian to the line profile in units of km s^{-1}, and R_{FWHM} is the FWHM extent of the galaxy measured from CO $(J = 1 \rightarrow 0)$ line emission in units of kpc. Here, we adopt the linewidth of HXMM05 excluding X-NE as Δv_{FWHM} and the average between the major and minor axes as the extent ($R_{FWHM} = 7.6$ kpc). We thus find an inclination-corrected dynamical mass of $M_{dyn}^{iso} = (3.89 \pm 1.09) \times 10^{12} \, M_\odot$, yielding a molecular gas mass fraction of $f_{gas}^{dyn,iso} = 4.3 \pm 2.9\%$ using M_{gas}^{HXMM05} for X-Main only and $5.3 \pm 2.4\%$ for the HXMM05 system. However, given the evidence of disk-like rotation for HXMM05, we consider the first dynamical mass estimate (i.e., M_{dyn}) to be more reliable.

5.5. *Star Formation Rate and Gas Surface Densities and the Spatially-resolved Star-formation Law*

The Schmidt-Kennicutt relation (i.e., the star-formation law) is an empirical relation relating SFR and gas sur-

---

[30] The M_{gas}/M_* ratio is susceptible to uncertainties in the α_{CO} conversion factor and in stellar mass. If we were to adopt a conversion factor of $4.6 \, M_\odot$ (K km pc^2)$^{-1}$, the gas-to-stellar mass ratio of HXMM05 would be consistent with the expected redshift evolution of the molecular gas mass content in galaxies (Geach et al. 2011).

[31] However, the gas reservoir would last 6 times longer if we had instead adopted $\alpha_{CO} = 4.6 \, M_\odot$ (K km pc^2)$^{-1}$ in deriving M_{gas}.

[32] The dominant systematic uncertainties in M_{dyn} are the uncertainties in the rotation velocity due to the potential presence of inflows or outflows, in the velocity dispersion, and in our assumption that HXMM05 is a thin disk with negligible scale height.

face densities as $\Sigma_{\mathrm{SFR}} \propto \Sigma_{\mathrm{gas}}^{N}$, where $N \simeq 1.4$ is established from measurements of different nearby galaxy populations (e.g., Schmidt 1959; Kennicutt 1998a, 2008). Based on the SFR of $2900_{-595}^{+750} M_{\odot}$ yr^{-1} and the sizes and flux ratio of XD1 and XD2 at $635\,\mu$m, we find star formation rates of SFR $= 1500$ and $860\,M_{\odot}$ yr^{-1} and SFR surface densities of $\Sigma_{\mathrm{SFR}}^{\mathrm{XD1}} = 210\,M_{\odot}$ yr^{-1} kpc^{-2} and $\Sigma_{\mathrm{SFR}}^{\mathrm{XD2}} = 120\,M_{\odot}$ yr^{-1} kpc^{-2} for XD1 and XD2, respectively. These SFR surface densities are elevated compared to those measured in the circumnuclear starburst regions of nearby galaxies (Kennicutt 1998b), consistent with the overall somewhat shorter gas depletion timescale but are much lower than those observed in high-z "maximal starburst"-like galaxies, such as the $z = 5.3$ SMG AzTEC-3, the $z = 5.7$ HyLIRG ADFS 27, and the $z = 6.3$ HFLS3 (Riechers et al. 2013, 2014b, 2017; Oteo et al. 2017b).

For the low surface brightness diffuse dust component, which is almost as extended as the [CII] line emission (Figure 8), we find a source-averaged SFR surface density of $\Sigma_{\mathrm{SFR}} = 10\,M_{\odot}$ yr^{-1} kpc^{-2} (or $60\,M_{\odot}$ yr^{-1} kpc^{-2} including the pair of nuclei). Based on the CO($J = 1 \rightarrow 0$) line-emitting source size of $(8.8 \pm 2.9) \times (6.4 \pm 3.5)$ kpc and the total molecular gas mass measured in the HXMM05 system, the molecular gas surface density is $\Sigma_{\mathrm{gas}} = (590 \pm 410) \times (\alpha_{\mathrm{CO}}/0.8)\,M_{\odot}$ pc^{-2}. We thus find that HXMM05 lies along the "starburst sequence" of the Schmidt-Kennicutt relation reported by Bouché et al. (2007). Accounting for uncertainties in SFR and gas surface densities, we find that HXMM05 lies in the same region of parameter space as the sub-regions of GN20 and the $z = 2.6$ SMG SMM J14011+0252 (Sharon et al. 2013; Hodge et al. 2015).

5.6. *CO Gas Excitation*

Due to the different physical conditions required to excite the various rotational transitions of CO, flux ratios between the low- and high-J CO lines are sensitive to the molecular gas volume densities and kinetic temperatures. With the data at hand (i.e., only four CO lines spanning the CO "ladder" up to $J = 10 \rightarrow 9$), we do not attempt to fit radiative transfer models to the observed line fluxes. Instead, we compare the line ratios measured in HXMM05 (Table 7) with those of other galaxy populations to study the connection between the SFR surface density and the gas excitation in HXMM05 (since SFR surface density is tightly linked to gas density, temperature, and line optical depths).

The global SFR of the HXMM05 system is comparable to those of the most luminous DSFGs known, but their different CO spectral line energy distribution (SLED) shapes indicate that the underlying physical conditions in their ISM may be different. As shown in Figure 13, the gas excitation of the HXMM05 system probed by transitions up to $J_{\mathrm{upper}} = 5$ is lower than those typically observed in nuclear starbursts, SMGs, and quasars, but is comparable to those observed in the outer disk of the Milky Way (despite HXMM05's much higher SFR), and those observed in high-z BzK disks. Such

a relatively modest gas excitation is in accord with the modest source-averaged SFR surface density of HXMM05 and its PDR gas conditions (§4.3) — i.e., its total SFR of $2900\,M_{\odot}$ yr^{-1} is spread across the entire disk (as seen in the co-spatial gas and FIR dust distribution), and its extended star formation is embedded within a medium with only moderate radiation flux and pressure.

Including the highest-J line probed with the data at hand ($J = 10 \rightarrow 9$), we find that the overall SLED shape (and thus gas excitation) of HXMM05 resembles that of the local merger-driven ULIRG Arp 220. This may suggest that the molecular ISM of the HXMM05 system is composed of (at least) two gas-phase components — a diffuse extended cold component and a dense warm component.

If we exclude X-NE, we find that the molecular gas in X-Main (i.e., grey symbols in Figure 13) is more highly excited than the system overall, which is comparable to other high-z DSFGs (e.g., Riechers 2011; Sharon et al. 2016). As noted in §3.1, the true CO ($J = 5 \rightarrow 4$) flux may be a factor of two higher. In this case, the excitation conditions of HXMM05 and X-Main would be consistent with (and possibly more excited than) those of other DSFGs. However, higher fidelity data are needed to confirm this scenario.
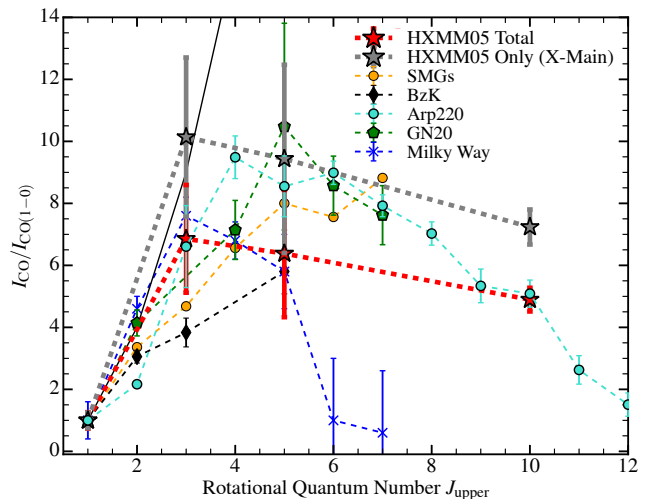

Figure 13. CO SLEDs of HXMM05 and other low- and high-z galaxies reported in the literature. Line fluxes are normalized to the CO ($J = 1 \rightarrow 0$) line. Red stars show the SLED of HXMM05 based on the total CO ($J = 1 \rightarrow 0$) flux (i.e, X-Main and X-NE; see Figure 2). Grey markers show the SLED of X-Main only, relative to its CO ($J = 1 \rightarrow 0$) flux. Solid black line shows the SLED expected for thermalized excitation and optically thick emission. Literature data are compiled from: Fixsen et al. (1999); Greve et al. (2009); Carilli et al. (2010); Rangwala et al. (2011); Danielson et al. (2011); Riechers et al. (2013); Carilli & Walter (2013); Bothwell et al. (2013); Kamenetzky et al. (2014); and Daddi et al. (2015).

5.7. *Morphology and Kinematics of the [CII] and CO Emission*

The cold molecular gas reservoir of HXMM05 is approximately $9\,\mathrm{kpc} \times 6\,\mathrm{kpc}$ in diameter, which is comparable to the mean size of nearby disk-like U/LIRGs (Ueda et al. 2014), and of ULIRGs in general (Gao & Solomon 1999). Simi-

larly extended gas reservoirs have also been observed in some other high-z galaxies (Daddi et al. 2010; Ivison et al. 2010a; Riechers et al. 2011a; Ivison et al. 2011; Hodge et al. 2012).

The CO $(J = 1 \rightarrow 0)$ FWHM linewidth of HXMM05 is much broader than those typically observed in "normal" star-forming galaxies at low- and high-redshifts, ULIRGs, and high-z gas-rich galaxies (Solomon et al. 1997; Solomon & Vanden Bout 2005; Daddi et al. 2010; Danielson et al. 2011; Ivison et al. 2011; Riechers et al. 2011a,b; Carilli & Walter 2013; Combes et al. 2013; Sharon et al. 2016), although galaxies with similarly broad line do exist (e.g., J13120+4242; Hainline et al. 2006; Riechers et al. 2011a). Similarly, the [CII] line of HXMM05 ($\Delta v = 667 \pm 46 \, \mathrm{km \, s^{-1}}$) is also broader than those seen in many other high-z galaxies apart from major mergers (e.g., Ivison et al. 2010b; Walter et al. 2012; Ivison et al. 2013; Riechers et al. 2013, 2014a; Neri et al. 2014; Rhoads et al. 2014).

The velocity dispersion traced by the [CII] line emission in HXMM05 is the highest in the central 0.''2 region, as seen in Figure 5. The higher dispersion at the center may indicate gas dynamics affected by late-stage merger activity, intense cold gas accretion/inflows, or enhanced turbulence caused by an undetected AGN, or the fact that systemic motions/radial velocities change abruptly in this region, where the velocity curve is also the steepest. We therefore estimate the gas dispersion in the extended part of HXMM05 based on the velocity dispersion observed in its outskirts, yielding $\sigma_v \simeq 75 \, \mathrm{km \, s^{-1}}$.

We estimate the v/σ stability parameter for HXMM05 using the maximum rotation velocity and the observed velocity dispersion of $\sigma = 75 \, \mathrm{km \, s^{-1}}$ (see §3.2), yielding $v/\sigma = 7 \pm 3$. This ratio is closer to those measured in nearby disk galaxies ($\simeq 10$) than in other high-z galaxies (e.g., Genzel et al. 2006; Förster Schreiber et al. 2006; Cresci et al. 2009; Gnerucci et al. 2011; Schreiber et al. 2017). This distinction may suggest that the ISM of HXMM05 is not as turbulent as other high-z galaxies studied to date (e.g., Law et al. 2009; Jones et al. 2010; Swinbank et al. 2011) — perhaps a result of its lower gas mass fraction[33] compared to other high-z galaxies. However, in most high-z studies with reliable v/σ estimates (requiring spatially resolved information), the ratio is typically derived from *stellar* kinematics (examples based on CO line emission are still limited in number; e.g., Swinbank et al. 2011). Determining the gas stability of galaxies by imaging their molecular gas reservoirs is more meaningful for characterizing their prospects for star formation, since molecular gas is the raw fuel for star formation. In other words, the stability of gas against gravitational collapse is more closely linked to star formation than the velocity structure of the existing stellar component, which may (re-)settle on a different timescale from the gas after perturbations.

5.8. *Dust*

5.8.1. *Morphology and Optical Depth*

HXMM05 remains undetected in deep UV and optical images, indicating that it is highly dust obscured, consistent with its rest-frame 158 μm optical depth of $\tau_\nu \simeq 1$ (determined from SED modeling; §4.1). This optical depth exceeds those of most "normal" star-forming galaxies and nearby disk galaxies, but is similar to that seen in Arp 220 and high-z starburst galaxies — e.g., HFLS3, AzTEC-3, and ADFS 27 (Riechers et al. 2013, 2014b, 2017).

The dust emission morphologies at 635 and 870 μm appear different (Figure 8). While two compact dust components are found to be embedded within an extended component at 635 μm, only one compact component coincides with XD1 at 870 μm. The second 635 μm dust peak, XD2, is 1.8 times fainter than XD1 at its peak flux (see Table 4). If XD1 and XD2 were to have the same peak flux ratio at 635 and 870 μm, we would expect a peak flux density of 6.2 mJy beam^{-1} for XD2 at 870 μm, which we would have detected at $>20 \, \sigma$ significance. Hence, the non-detection of XD2 at 870 μm may be a result of the lower dust column density at 870 μm, where the emission is optically thin on average based on[34] the best-fit dust SED model ($\tau_\nu = 0.54$).

5.8.2. *Interpretation of the compact dust components*

The compact dust components, XD1 and XD2, detected at 635 μm could be two regions of intense star formation, or the remnant cores from a previous merger (e.g., Johansson et al. 2009). At the positions of the double nuclei, the velocity field of HXMM05 is the steepest (see markers in Figure 5), but we find no obvious signs of a misaligned velocity gradient at their positions, which would be expected for the latter scenario. However, the velocity field is only a first-order representation of the kinematics of a galaxy, since it is calculated based on intensity-weighted LOS velocities and is affected by the limited spatial resolution of the data (similarly for the velocity dispersion map). Thus, it will not capture the full kinematics in the system. As such, we cannot rule out the possibility that the double nuclei may be the cores of a pair of progenitor galaxies, where the gas disk may have reconfigured itself into rotation already (e.g., Springel & Hernquist 2005; Robertson et al. 2006; Narayanan et al. 2008; Robertson & Bullock 2008; Hopkins et al. 2009). Such a scenario would be reminiscent of the nearby ULIRG Arp 220 (e.g., Sakamoto et al. 2008; Scoville et al. 2017), but with a greater separation between the pair in HXMM05.

Alternatively, if the dust peaks were truly giant star-forming "clumps" that are virialized, we would expect their velocity dispersions to be $\sigma_v \simeq 40 \, \mathrm{km \, s^{-1}}$ or $\simeq 400 \, \mathrm{km \, s^{-1}}$ based on the size-linewidth relations found for local GMCs in a quiescent environment or the Galactic center, respectively (Larson

---

[33] Compared based on $f_{\mathrm{gas}}^{\mathrm{dyn,iso}}$.

[34] The optical depth derived from a galaxy-averaged SED model is luminosity-weighted, and thus, biased toward compact dust components. The true optical depth is likely to be even lower in the outskirts of a galaxy.

1981). As shown in Figure 5, the observed velocity dispersion in the nuclei of HXMM05 is $160-200 \, \mathrm{km \, s^{-1}}$. Thus, the dust peaks are unlikely to be virialized clumps.

Similarly, a scenario in which XD1 and XD2 correspond to the "*twin* peaks" produced in response to an $m = 2$ (i.e., bar or oval) perturbation (see e.g., Kenney et al. 1992) is disfavored for two main reasons: the lack of obvious non-circular motions (§4.2.1), and the pronounced asymmetry in the $635/870 \, \mu$m flux ratio of XD1 and XD2 (i.e., implying differences in their optical depths and dust column densities).

5.9. *[CII] and FIR Luminosity Ratio*

The $L_{\rm [CII]}/L_{\rm FIR}$ ratio measures the fraction of far-UV photons that is heating up the gas versus that deposited onto dust grains. We find a $L_{\rm [CII]}/L_{\rm FIR}$ ratio of $0.20 \pm 0.03\%$ for HXMM05. Thus, HXMM05 lies in the same region of parameter space as nearby star-forming galaxies and LIRGs, despite its two orders of magnitude higher $L_{\rm FIR}$ (e.g., Stacey et al. 2010). This ratio is consistent with those measured in other high-z star formation-dominated galaxies with similar far-IR luminosities in the $L_{\rm [CII]}/L_{\rm FIR} - L_{\rm FIR}$ plane (cf. nearby ULIRGs and high-z quasars; Malhotra et al. 2001; Hailey-Dunsheath et al. 2010; Stacey et al. 2010; Wang et al. 2013; Díaz-Santos et al. 2013; Zhang et al. 2018b), suggesting that HXMM05 is dominated by extended star formation rather than a compact starbursts or AGN (see also §2.6.9). This evidence is consistent with the extent observed in its gas and dust emission.

5.10. *Spatially Resolved $L_{\rm [CII]}/L_{\rm FIR}$ Map and Star Formation*
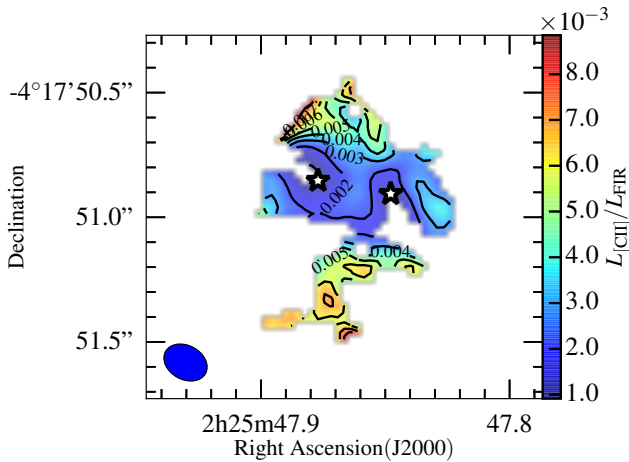
Figure 14. [CII]-to-FIR luminosity ratio map of X-Main (X-NE is outside the field of view shown here). We clipped the [CII] and continuum maps at a 3σ level here. The spatially resolved $L_{\rm FIR}$ is derived using the $635 \, \mu$m continuum image. A negative gradient is observed toward the center of HXMM05 and is most likely caused by an increase in the radiation field intensity (see Figure 15 and §5.10). Star symbols mark the positions of XD1 and XD2.

We investigate the spatially resolved [CII]-to-FIR luminosity ratio in HXMM05 on 1-kpc scale to examine the connection between SFR and [CII] surface densities. To create the surface density plots in Figures 14 and 15, we clipped both

the [CII] and the $635 \, \mu$m continuum maps at 3σ[35]. Essentially, the notion of using the [CII] luminosity as a proxy for SFR relies on the assumption that [CII] dominates the cooling budget of the neutral ISM, in which heating is dominated by the photoelectric effect of UV photons from young and massive stars. We show the $\Sigma_{\rm SFR} - \Sigma_{\rm [CII]}$ relation for HXMM05 in the left panel of Figure 15. The large scatter suggests that [CII] emission traces both star-forming regions and "diffuse" gas reservoirs. The trend of decreasing $L_{\rm [CII]}/L_{\rm FIR}$ at high $\Sigma_{\rm SFR}$ suggests that the former is suppressed in compact, high-SFR surface density regions (Figure 14). On the other hand, we find a tighter relation between $\Sigma_{\rm [CII]}/\Sigma_{\rm FIR}$ and $\Sigma_{\rm FIR}$, as shown in the right panel of Figure 15.

We fit power-laws of the forms $\Sigma_{\rm SFR} = A\Sigma_{\rm [CII]}^N$ and $L_{\rm [CII]}/L_{\rm FIR} = A\Sigma_{\rm FIR}^N$ to our data for HXMM05, and find the following best-fit relations:

$$\log\left(\frac{\Sigma_{\rm SFR}}{M_\odot \, \mathrm{yr^{-1} \, pc^{-2}}}\right) = -3.0 \, (\pm 0.3) \, +$$
$$1.4 \, (\pm 0.1) \times \log\left(\frac{\Sigma_{\rm [CII]}}{L_\odot \, \mathrm{pc^{-2}}}\right); \quad (7)$$

and

$$\log\left(\frac{L_{\rm [CII]}}{L_{\rm FIR}}\right) = 5.91 \, (\pm 0.14) - 0.81 \, (\pm 0.01) \times \log\left(\frac{\Sigma_{\rm FIR}}{L_\odot \, \mathrm{kpc^{-2}}}\right). \quad (8)$$

The slope of the former relation coincidentally resembles the slope of the Schmidt-Kennicutt relation for the CO $(J = 1 \to 0)$ line on kpc scales, albeit with a large scatter (Kennicutt 1998b). The slope of the latter relation is steeper than those reported by Díaz-Santos et al. (2013, 2017) for nearby ULIRGs, perhaps due to the different tracers used. The latter authors use $L_{\rm IR}$ and source size measured at $24 \, \mu$m to derive the FIR surface density, whereas we use $L_{\rm FIR}$ and FIR size (or pixels) measured at rest-frame $158 \, \mu$m for HXMM05. The steeper relation found in HXMM05 can also be understood if we were to assume that its outer region, where the $L_{\rm [CII]}/L_{\rm FIR}$ ratio is the highest, has a lower metallicity (and thus, a higher photoelectric heating efficiency). In any case, the tight $L_{\rm [CII]}/L_{\rm FIR} - \Sigma_{\rm FIR}$ relationship is consistent with the notion that the two quantities are connected through the the local FUV radiation field intensity.

We find that the $L_{\rm [CII]}/L_{\rm FIR}$ ratio of HXMM05 decreases toward the center, as shown in the spatially resolved map in Figure 14. Such a negative gradient has been observed in nearby star-forming galaxies (e.g., Kramer et al. 2013; Smith et al. 2017) and U/LIRGs (Díaz-Santos et al. 2014). The deficit at the center may be explained by a higher dust temperature (see §3.4) and a more intense radiation field at the center (given that $G_0 \propto R^{-2}$). In addition, the gas density at the center is likely to exceed the critical density of [CII], where collisional de-excitation dominates and saturates the [CII] emission (Luh-

---

[35] We also test our results with less clipping (at 1σ) to confirm that the trends and relationships found are not artificial or biased because of "excessive" clipping.
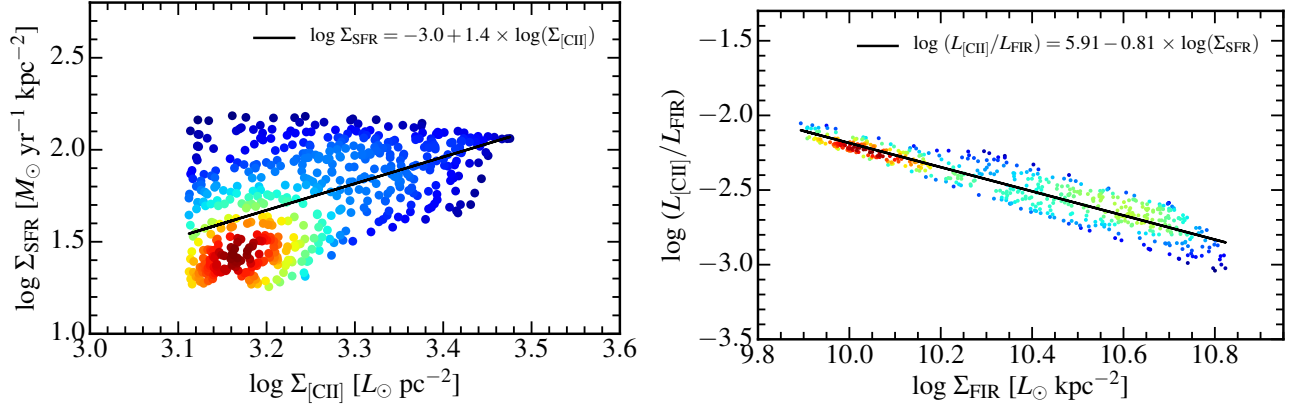
Figure 15. Relations based on a pixel-by-pixel analysis, scaling the quantities to their respective units shown. Left: Σ_{SFR} and $\Sigma_{\mathrm{[CII]}}$ relation from pixel measurements from the [CII]/635 μm continuum ratio map (§5.10); a large scatter is seen between the two quantities. Right: $L_{\mathrm{[CII]}}/L_{\mathrm{FIR}}$ as a function of L_{FIR} surface density (Σ_{FIR}). To derive this surface density map, we clipped both [CII] and continuum maps at a 3σ level. Colors in both panels represent the density of points; approximately bins of 50 points are correlated, based on the beam size of the data.

man et al. 1998; Malhotra et al. 1997; Goldsmith et al. 2012). This effect also explains the decreasing $L_{\mathrm{[CII]}}/L_{\mathrm{FIR}}$ ratio found with increasing FIR surface densities in the $L_{\mathrm{[CII]}}/L_{\mathrm{FIR}} - \Sigma_{\mathrm{FIR}}$ relation (Figure 15).

5.11. *HXMM05 in the Context of High-z Galaxy Populations*

HXMM05 is one of the most IR-luminous galaxies known at high redshift. Given its IR luminosity of $L_{\mathrm{IR}} = 4 \times 10^{13} L_\odot$, it can be classified as a HyLIRG. However, we find that its ISM properties differ from those observed in some other un-lensed HyLIRGs studied to date. For instance, both the gas and SFR surface densities of HXMM05 are much lower than those observed in GN20 and the $z = 5.7$ binary HyLIRG ADFS 27 (Hodge et al. 2012; Riechers et al. 2017), but are comparable to those of the $z = 2.4$ HyLIRG merger HATLAS J084933 and the sub-regions of GN20 (Ivison et al. 2013; Hodge et al. 2015), suggesting that the star formation in HXMM05 is relatively modest compared to "maximum"-starburst-like HyLIRGs.

Given the dynamical mass, stellar mass, and sSFR of HXMM05, it is among the most massive galaxies known at $z = 3$. However, as discussed in §3.4, HXMM05 was discovered with *Herschel*/SPIRE observations at submillimeter wavelengths and remains undetected in deep UV and optical observations. It therefore differs from other high-z massive disk galaxy populations, such as those typically selected in the UV, optical, and NIR wavebands by applying the U-, B-, G-, R-, z-, K-band color-selection and the Lyman Break "dropout" technique (i.e., BzK, BM/BX, and LBG; Steidel et al. 1996; Adelberger et al. 2004; Steidel et al. 2004; Daddi et al. 2004), in that it has a larger dust content, which may suggest different evolutionary histories for these high-z populations.

The molecular gas extent, kinematics, gas excitation, SFR, dust mass, SFE, SFR surface density, and metallicity of HXMM05 are similar to those of GN20. This agreement suggests that HXMM05 and GN20 may belong to the same class of DSFG. The finding of such rare massive disk galaxies at $z \sim 3$ could be consistent with model predictions that disk-

wide star formation plays an important role for some of the most massive DSFGs at early epochs, whether as a phase in a merger event or (Hayward et al. 2013) independent of a major merger altogether[36].

6. IMPLICATIONS ON THE FORMATION SCENARIOS OF HXMM05 — MAJOR MERGER AND COLD MODE ACCRETION

With a SFR of 2900 $M_\odot$ yr^{-1} and a stellar mass of $10^{12} M_\odot$, distributed across a rotating disk 9 kpc in diameter, HXMM05 is a massive rotation-dominated star-forming galaxy. One of the main goals in studying high-z star-forming galaxies is to examine and understand what drives their high SFRs. A critical question concerns whether an interaction is required to drive the high SFRs observed in high-z starbursting DSFGs — which would put them in a transient phase — or whether DSFGs are just a massive galaxy population undergoing "quiescent" star formation, but at higher rates due simply to their higher masses and/or gas mass fractions compared to nearby and low-mass galaxies. Previous theoretical and observational studies have suggested that star formation in the most massive starburst-dominated DSFGs is likely triggered by major mergers, whereas less massive systems could be triggered by gravitational instability as a result of their high gas mass fractions (e.g., Chapman et al. 2003; Engel et al. 2010; Narayanan et al. 2010; Hayward et al. 2011, 2013; Riechers et al. 2017).

In cosmological N-body zoom-in and hydrodynamic simulations, massive galaxies with stellar masses similar to that of HXMM05, albeit rare, can be formed quickly by $z = 6$ via multiple gas-rich major mergers (Li et al. 2007; Davé et al. 2010, see also Ruszkowski & Springel 2009). From a theoretical point of view, it is thus conceivable that HXMM05 may have recently experienced a major merger that would explain its broad CO lines, high SFR, large molecular gas mass, and its 3 kpc size double nuclei observed at 635 μm. In this scenario, the double nuclei may correspond to two compact

---

[36] This statement does not explicitly address the relevance of merger activity in the overall evolution of massive disks.

obscured starburst regions triggered by massive gas inflows, or to the remnant cores of two similar mass progenitor galaxies (Johansson et al. 2009). On the other hand, the observed spatial extent, velocity gradient, G_0, and gas surface density observed in HXMM05 are more consistent with a rotation-dominated "normal" star-forming galaxy, suggesting that additional mechanisms may be at work to form a system like HXMM05.

In the standard model of dissipational disk formation, infant disk galaxies form from the gas that is infalling into hierarchically growing dark matter halos. However, since a substantial fraction of the angular momentum of gas is lost to the surrounding halo through dynamical friction (up to 90%) while it configures itself into a rotationally supported disk in the inner portion of the dark matter halo, disks are an order of magnitude smaller than those observed (also known as the angular momentum "catastrophe"; e.g., Steinmetz & Navarro 1999). In this formation paradigm, a massive extended disk like HXMM05 is quite unexpected at $z = 3$ (only about 2 Gyr after the Big Bang). While feedback and the continuation of tidal torquing and accretion of satellite galaxies/minor mergers have been proposed to resolve the disagreement between models and observations, as they can prevent the gas from over-cooling and losing its angular momentum (e.g., Sommer-Larsen & Dolgov 2001; Robertson et al. 2004; Scannapieco et al. 2008; Zavala et al. 2008), it remains unclear whether minor mergers[37] alone could increase the angular momentum sufficiently to explain the properties and number density of disk galaxies observed (e.g., Vitvitska et al. 2002).

In recent years, the cold mode accretion formation model has been put forward as an alternative mechanism capable of driving the high SFRs seen in high-z gas-rich star-forming galaxies, which may also explain the discrepancy with major mergers (i.e., there are not enough major mergers in models to explain all DSFGs as merger-driven starbursts; Kereš et al. 2005; Dekel et al. 2009a,b; Davé et al. 2010; see also Narayanan et al. 2015 and Lacey et al. 2016). Since cold streams can provide additional angular momentum, extended gas-rich disk galaxies with kpc-scale star formation can be explained naturally (Kereš et al. 2005; Dekel et al. 2009a).

Given that some properties of HXMM05 are consistent with the major merger scenario and others are consistent with the cold mode accretion scenario, it is conceivable that both mechanisms together are important to give rise to a galaxy like HXMM05, which perhaps is similar to the case of GN20 (see Carilli et al. 2010).

7. SUMMARY AND CONCLUSIONS

We determine the redshift and gas excitation of the *Herschel*-selected DSFG HXMM05 at $z = 2.9850 \pm 0.0009$ by observing its CO($J = 1 \rightarrow 0$; $3 \rightarrow 2$; $5 \rightarrow 4$; $10 \rightarrow 9$) line emission. We image its gas reservoir and dust-obscured star for-

mation on 1.2 kpc scales using [CII] line and dust continuum emission.

We detect a companion galaxy (hereafter X-NE) about 20 kpc NE of the main component of HXMM05 (hereafter X-Main) in CO($J = 1 \rightarrow 0$) and [CII] line emission at a redshift close to X-Main ($\Delta v = -535 \pm 55 \text{ km s}^{-1}$). X-NE is also detected in the UV, optical, and NIR continuum emission. Based on the CO($J = 1 \rightarrow 0$) line flux, we infer a total molecular gas mass of $M_{\text{gas}}^{\text{total}} = (2.12 \pm 0.71) \times (\alpha_{\text{CO}}/0.8) \times 10^{11} \, M_\odot$ residing in the HXMM05 system (composed of X-NE and X-Main), yielding a gas mass fraction of $f_{\text{gas}}^{\text{dyn}} = 33 \pm 15\%$.

Based on the CO($J = 1 \rightarrow 0$) and [CII] line data, the velocity structure of X-Main is consistent with a rotating disk, with a diameter of ~ 9 kpc. Thus, the gas reservoir of HXMM05 is more extended than those typically observed in high-z DSFGs and quasars, but comparable to those observed in high-z "main-sequence" galaxies and the $z = 4$ starburst galaxy GN20 (Carilli et al. 2010; Hodge et al. 2015). We find that the widths of its CO($J = 1 \rightarrow 0$; $10 \rightarrow 9$) and [CII] lines are broader than those typically observed in "normal" star-forming galaxies, ULIRGs, and high-z SMGs, but comparable to those observed in the more extreme systems (e.g., J13120+4242 and G09v124; Riechers et al. 2011a; Ivison et al. 2013). We find that the overall gas excitation of HXMM05 resembles that of the nearby galaxy merger Arp 220. The shape of the CO excitation ladder (i.e., SLED) suggests that the molecular ISM of HXMM05 may consist of (at least) two gas phases — a diffuse extended cold component and a dense compact warm component.

The X-Main component of the HXMM05 system remains undetected in deep UV and optical observations, indicating that it is highly dust obscured. We find a pair of compact dust components (XD1 and XD2) in the dust continuum emission at 635 μm, which are about 3 kpc across each and are separated by 2 kpc. The pair is embedded within an extended dust component, which also appears to be as extended as the CO($J = 1 \rightarrow 0$) and [CII] line emission. The brightness temperatures of the nuclei suggest that they may be warmer, more optically thick, and/or with higher beam filling factors than the extended dust component. We find that the source-averaged FUV radiation field intensity of HXMM05 is around 200 times stronger than that of the local Galactic interstellar medium, but is comparable to those observed in nearby star-forming galaxies and other DSFGs. The PDR properties of HXMM05 together with its gas properties and excitation are indicative of galaxy-wide star formation, consistent with its extended gas and dust emission observed (as opposed to those typically observed in compact starburst galaxies).

We find a stellar mass of $M_* \simeq 10^{12} \, M_\odot$ and an SFR of $\simeq 2900 \, M_\odot \text{ yr}^{-1}$ for HXMM05 from SED modeling, consistent with it being one of the most massive star-forming galaxies at $z = 3$. We also find source-averaged SFR and molecular gas surface densities of $\Sigma_{\text{SFR}} = 10 - 60 \, M_\odot \text{ yr}^{-1} \text{ kpc}^{-2}$ and $\Sigma_{\text{gas}} = 590 \times (\alpha_{\text{CO}}/0.8) \, M_\odot \text{ pc}^{-2}$. Thus, HXMM05 lies

---

[37] Major mergers would take a few Gyr to form an extended disk again from two progenitor disks, if ever (e.g., Governato et al. 2009).

along the "starburst sequence" of the Schmidt-Kennicutt relation (e.g., Bouché et al. 2007), similar to the sub-regions of GN20 and the $z \sim 2.6$ SMG SMM J14011+0252 (Sharon et al. 2013; Hodge et al. 2015). This locus corresponds to an elevated SFE compared to other SFMS galaxies. The SFR surface densities for the double nuclei are elevated compared to those observed in the circumnuclear starburst regions of nearby galaxies (Kennicutt 1998b), but are much lower than those observed in other (not strongly lensed) high-z HyLIRGs ("maximum starbursts"; e.g., Riechers et al. 2013, 2014b, 2017; Oteo et al. 2017b).

A large scatter seen in the $\Sigma_{SFR} - \Sigma_{[CII]}$ relation for HXMM05 on 1 kpc scale suggests that its [CII] emission traces both star-forming regions and "diffuse" gas reservoirs. We find a tighter relation between $L_{[CII]}/L_{FIR}$ and Σ_{SFR} across HXMM05, which is consistent with our understanding that the two quantities are connected through the local FUV radiation field intensity (e.g., Tielens & Hollenbach 1985, and references therein). We find that the $L_{[CII]}/L_{FIR}$ ratio is "suppressed" at high SFR surface densities (e.g., near the center of HXMM05), which is suggestive of a stronger UV radiation field and warmer dust emission there. On the other hand, the source-averaged $L_{[CII]}/L_{FIR}$ ratio of HXMM05 is comparable to those of nearby star-forming galaxies and LIRGs rather than nearby ULIRGs and quasars, despite its two orders of magnitude higher L_{FIR}.

The scatter observed in the spatially resolved and galaxy-integrated [CII] and FIR luminosity relations for HXMM05 are consistent with our understanding that $L_{[CII]}$ and SFR are not related linearly. The spatially resolved data presented in this paper thus confirm the speculation put forward by Stacey et al. (2010) based on unresolved observations: that high-z DSFGs are not simple scaled-up ULIRGs and that starburst-dominated DSFGs can be much more extended than ULIRGs, which is also consistent with previous findings of spatially extended CO emission (e.g., Riechers et al. 2011a; Ivison et al. 2011).

While rotationally-supported clumps may yield velocity gradients (§5.8.2), we find no evidence of such with the data at hand, in spite of the pair of dust peaks identified. Even in the merging clump scenario (e.g., in late stage merger), it is unlikely for the clumps to have a huge impact on the global scale across the entire galaxy as to cause a monotonic velocity gradient over ~ 9 kpc across, especially given the observed centrally peaked velocity dispersion observed in the [CII] data, which is relatively uniform outside the central ~ 1.2 kpc[38]. Another piece of evidence disfavoring HXMM05 from being strictly a dispersion-dominated merger system comes from the fact that the potential merger candidates (the pair of dust peaks) are oriented almost-perpendicular to the velocity gradient. We further quantified the disk-like kinematics of HXMM05 based on the higher order Fourier co-

efficients of the harmonic decomposition (§4.2.1), which are found to be insignificant compared to the $m = 0$ term. We thus interpret HXMM05 to be a rotating disk[39].

The disk-like kinematics, extended star formation, high SFR and M_*, and gas and SFR surface densities of HXMM05 are quite similar to those of GN20 (Hodge et al. 2012, 2015), suggesting that the two may correspond to the same class of DSFG — massive extended rotating disks with highly dust-obscured star formation.

HXMM05 can be classified as a HyLIRG, making it one of the most IR-luminous galaxies known. In a sample of the brightest high-z DSFGs discovered in the 95 deg^2 surveyed by HerMES, only around 10% appear to be intrinsically comparably luminous, corresponding to a surface density of only 0.03 deg^{-2} (Bussmann et al. 2015). In fact, the stellar mass function also suggests that massive galaxies like HXMM05 are very rare at $z = 3$ (Davé et al. 2010; Schreiber et al. 2015). In the framework of the hierarchical formation model, one would expect a massive galaxy like HXMM05 to form via major mergers, given its high SFR and M_*. The two compact dust nuclei and enhanced central velocity dispersion as well as the detection of a companion galaxy at only 20 kpc away may be consistent with such a scenario. However, its extended massive gas disk, monotonic velocity gradient, G_0, and gas and SFR surface densities at $z = 3$ suggest additional mechanisms such as proposed in the cold mode accretion model may also play an important role in shaping the existence and subsequent evolution of massive DSFGs. HXMM05 could thus be a rare example of such system showing both mechanisms at play.

---

[38] Approximately the beam size.

[39] Note that this does not rule out the possibility that the disk is part of a merger.

Adelberger, K. L., Steidel, C. C., Shapley, A. E., et al. 2004, ApJ, 607, 226

Aravena, M., Hodge, J. A., Wagg, J., et al. 2014, MNRAS, 442, 558

Astropy Collaboration, Robitaille, T. P., Tollerud, E. J., et al. 2013, A&A, 558, A33

Begeman, K. G. 1989, A&A, 223, 47

Bothwell, M. S., Smail, I., Chapman, S. C., et al. 2013, MNRAS, 429, 3047

Bouché, N., Cresci, G., Davies, R., et al. 2007, ApJ, 671, 303

Braine, J., Gratier, P., Kramer, C., et al. 2012, A&A, 544, A55

Bussmann, R. S., Riechers, D., Fialkov, A., et al. 2015, ApJ, 812, 43

Calanog, J. A., Fu, H., Cooray, A., et al. 2014, ApJ, 797, 138

Calura, F., Pozzi, F., Cresci, G., et al. 2017, MNRAS, 465, 54

Carilli, C. L., & Walter, F. 2013, ARA&A, 51, 105

Carilli, C. L., Daddi, E., Riechers, D., et al. 2010, ApJ, 714, 1407

Carral, P., Hollenbach, D. J., Lord, S. D., et al. 1994, ApJ, 423, 223

Casey, C. M., Narayanan, D., & Cooray, A. 2014, Phys. Rep., 541, 45

Chabrier, G. 2003, PASP, 115, 763

Chapman, S. C., Windhorst, R., Odewahn, S., Yan, H., & Conselice, C. 2003, ApJ, 599, 92

Chemin, L., Carignan, C., & Foster, T. 2009, ApJ, 705, 1395

Chiappetti, L., Tajer, M., Trinchieri, G., et al. 2005, A&A, 439, 413

Colbert, J. W., Malkan, M. A., Clegg, P. E., et al. 1999, ApJ, 511, 721

Combes, F., García-Burillo, S., Braine, J., et al. 2013, A&A, 550, A41

Courteau, S. 1997, AJ, 114, 2402

Cresci, G., Hicks, E. K. S., Genzel, R., et al. 2009, ApJ, 697, 115

da Cunha, E., Charlot, S., & Elbaz, D. 2008, MNRAS, 388, 1595

da Cunha, E., Walter, F., Smail, I. R., et al. 2015, ApJ, 806, 110

Daddi, E., Dannerbauer, H., Elbaz, D., et al. 2008, ApJ, 673, L21

Daddi, E., Cimatti, A., Renzini, A., et al. 2004, ApJ, 600, L127

Daddi, E., Bournaud, F., Walter, F., et al. 2010, ApJ, 713, 686

Daddi, E., Dannerbauer, H., Liu, D., et al. 2015, A&A, 577, A46

Danielson, A. L. R., Swinbank, A. M., Smail, I., et al. 2011, MNRAS, 410, 1687

Davé, R., Finlator, K., & Oppenheimer, B. D. 2012, MNRAS, 421, 98

Davé, R., Finlator, K., Oppenheimer, B. D., et al. 2010, MNRAS,

404, 1355

Decarli, R., Walter, F., Aravena, M., et al. 2016, ApJ, 833, 70

Dekel, A., Sari, R., & Ceverino, D. 2009a, ApJ, 703, 785

Dekel, A., Birnboim, Y., Engel, G., et al. 2009b, Nature, 457, 451

Di Teodoro, E. M., & Fraternali, F. 2015, MNRAS, 451, 3021

Díaz-Santos, T., Armus, L., Charmandaris, V., et al. 2013, ApJ, 774, 68

—. 2014, ApJ, 788, L17

—. 2017, ApJ, 846, 32

Diolaiti, E., Bendinelli, O., Bonaccini, D., et al. 2000, A&AS, 147, 335

Donley, J. L., Rieke, G. H., Pérez-González, P. G., & Barro, G. 2008, ApJ, 687, 111

Donley, J. L., Rieke, G. H., Pérez-González, P. G., Rigby, J. R., & Alonso-Herrero, A. 2007, ApJ, 660, 167

Dowell, C. D., Conley, A., Glenn, J., et al. 2014, ApJ, 780, 75

Downes, D., & Solomon, P. M. 1998, ApJ, 507, 615

Draine, B. T., & Li, A. 2007, ApJ, 657, 810

Dunne, L., Eales, S. A., & Edmunds, M. G. 2003, MNRAS, 341, 589

Dunne, L., Gomez, H. L., da Cunha, E., et al. 2011, MNRAS, 417, 1510

Elson, E. C. 2014, MNRAS, 437, 3736

Elvis, M., Maccacaro, T., Wilson, A. S., et al. 1978, MNRAS, 183, 129

Engel, H., Tacconi, L. J., Davies, R. I., et al. 2010, ApJ, 724, 233

Fall, S. M., & Efstathiou, G. 1980, MNRAS, 193, 189

Fixsen, D. J., Bennett, C. L., & Mather, J. C. 1999, ApJ, 526, 207

Förster Schreiber, N. M., Genzel, R., Lehnert, M. D., et al. 2006, ApJ, 645, 1062

Fu, H., Cooray, A., Feruglio, C., et al. 2013, Nature, 498, 338

Gao, Y., & Solomon, P. M. 1999, ApJ, 512, L99

—. 2004, ApJ, 606, 271

Geach, J. E., Smail, I., Moran, S. M., et al. 2011, ApJ, 730, L19

Genzel, R., Tacconi, L. J., Eisenhauer, F., et al. 2006, Nature, 442, 786

Genzel, R., Tacconi, L. J., Combes, F., et al. 2012, ApJ, 746, 69

Genzel, R., Schreiber, N. M. F., Übler, H., et al. 2017, Nature, 543, 397

Gnerucci, A., Marconi, A., Cresci, G., et al. 2011, A&A, 528, A88

Goldsmith, P. F., Langer, W. D., Pineda, J. L., & Velusamy, T. 2012, ApJS, 203, 13

Governato, F., Brook, C. B., Brooks, A. M., et al. 2009, MNRAS, 398, 312

Greve, T. R., Papadopoulos, P. P., Gao, Y., & Radford, S. J. E. 2009, ApJ, 692, 1432

Hailey-Dunsheath, S., Nikola, T., Stacey, G. J., et al. 2010, ApJ, 714, L162

Hainline, L. J., Blain, A. W., Greve, T. R., et al. 2006, ApJ, 650, 614

Hallenbeck, G., Huang, S., Spekkens, K., et al. 2014, AJ, 148, 69

Hayward, C. C., Kereš, D., Jonsson, P., et al. 2011, ApJ, 743, 159

Hayward, C. C., Narayanan, D., Kereš, D., et al. 2013, MNRAS, 428, 2529

Hayward, C. C., & Smith, D. J. B. 2015, MNRAS, 446, 1512

Hinshaw, G., Larson, D., Komatsu, E., et al. 2013, ApJS, 208, 19

Hodge, J. A., Carilli, C. L., Walter, F., et al. 2012, ApJ, 760, 11

Hodge, J. A., Riechers, D., Decarli, R., et al. 2015, ApJ, 798, L18

Hollenbach, D., Kaufman, M. J., Neufeld, D., Wolfire, M., & Goicoechea, J. R. 2012, ApJ, 754, 105

Hollenbach, D. J., & Tielens, A. G. G. M. 1999, Reviews of Modern Physics, 71, 173

Hopkins, P. F., Cox, T. J., Younger, J. D., & Hernquist, L. 2009, ApJ, 691, 1168

Hudelot, P., Cuillandre, J.-C., Withington, K., et al. 2012, VizieR Online Data Catalog, 2317

Ivison, R. J., Papadopoulos, P. P., Smail, I., et al. 2011, MNRAS, 412, 1913

Ivison, R. J., Smail, I., Papadopoulos, P. P., et al. 2010a, MNRAS, 404, 198

Ivison, R. J., Swinbank, A. M., Swinyard, B., et al. 2010b, A&A, 518, L35

Ivison, R. J., Swinbank, A. M., Smail, I., et al. 2013, ApJ, 772, 137

Jarvis, M. J., Bonfield, D. G., Bruce, V. A., et al. 2013, MNRAS, 428, 1281

Johansson, P. H., Naab, T., & Burkert, A. 2009, ApJ, 690, 802

Jones, T., Ellis, R., Jullo, E., & Richard, J. 2010, ApJ, 725, L176

Jovanović, M. 2017, MNRAS, 469, 3564

Kamenetzky, J., Rangwala, N., Glenn, J., Maloney, P. R., & Conley, A. 2014, ApJ, 795, 174

Kannappan, S. J., & Gawiser, E. 2007, ApJ, 657, L5

Kauffmann, G., & Charlot, S. 1998, MNRAS, 297, L23

Kaufman, M. J., Wolfire, M. G., & Hollenbach, D. J. 2006, ApJ, 644, 283

Kaufman, M. J., Wolfire, M. G., Hollenbach, D. J., & Luhman, M. L. 1999, ApJ, 527, 795

Kenney, J. D. P., Wilson, C. D., Scoville, N. Z., Devereux, N. A., & Young, J. S. 1992, ApJ, 395, L79

Kennicutt, Jr., R. C. 1998a, ARA&A, 36, 189

—. 1998b, ApJ, 498, 541

Kennicutt, Jr., R. C. 2008, in Astronomical Society of the Pacific Conference Series, Vol. 390, Pathways Through an Eclectic Universe, ed. J. H. Knapen, T. J. Mahoney, & A. Vazdekis, 149

Kereš, D., Katz, N., Weinberg, D. H., & Davé, R. 2005, MNRAS, 363, 2

Kewley, L. J., & Dopita, M. A. 2002, ApJS, 142, 35

Kewley, L. J., & Ellison, S. L. 2008, ApJ, 681, 1183

Krajnović, D., Cappellari, M., de Zeeuw, P. T., & Copin, Y. 2006, MNRAS, 366, 787

Kramer, C., Abreu-Vicente, J., García-Burillo, S., et al. 2013, A&A, 553, A114

Lacey, C. G., Baugh, C. M., Frenk, C. S., et al. 2008, MNRAS, 385, 1155

—. 2016, MNRAS, 462, 3854

Lang, P., Förster Schreiber, N. M., Genzel, R., et al. 2017, ApJ, 840, 92

Larson, R. B. 1981, MNRAS, 194, 809

Law, D. R., Steidel, C. C., Erb, D. K., et al. 2009, ApJ, 697, 2057

Le Petit, F., Nehmé, C., Le Bourlot, J., & Roueff, E. 2006, ApJS, 164, 506

Lehnert, M. D., van Driel, W., Le Tiran, L., Di Matteo, P., & Haywood, M. 2015, A&A, 577, A112

Leroy, A. K., Walter, F., Brinks, E., et al. 2008, AJ, 136, 2782

Leroy, A. K., Bolatto, A., Gordon, K., et al. 2011, ApJ, 737, 12

Leroy, A. K., Walter, F., Sandstrom, K., et al. 2013, AJ, 146, 19

Leung, T. K. D., Riechers, D. A., & Pavesi, R. 2017, ApJ, 836, 180

Li, Y., Hernquist, L., Robertson, B., et al. 2007, ApJ, 665, 187

Lilly, S. J., Carollo, C. M., Pipino, A., Renzini, A., & Peng, Y. 2013, ApJ, 772, 119

Lonsdale, C. J., Smith, H. E., Rowan-Robinson, M., et al. 2003, PASP, 115, 897

Luhman, M. L., Satyapal, S., Fischer, J., et al. 1998, ApJ, 504, L11

Madau, P., & Dickinson, M. 2014, ARA&A, 52, 415

Magdis, G. E., Elbaz, D., Dickinson, M., et al. 2011, A&A, 534, A15

Magdis, G. E., Daddi, E., Sargent, M., et al. 2012, ApJ, 758, L9

Malhotra, S., Helou, G., Stacey, G., et al. 1997, ApJ, 491, L27

Malhotra, S., Kaufman, M. J., Hollenbach, D., et al. 2001, ApJ, 561, 766

Mannucci, F., Cresci, G., Maiolino, R., Marconi, A., & Gnerucci, A. 2010, MNRAS, 408, 2115

Martin, D. C., Fanson, J., Schiminovich, D., et al. 2005, ApJ, 619, L1

Mauduit, J.-C., Lacy, M., Farrah, D., et al. 2012, PASP, 124, 714

McGaugh, S. S., & Schombert, J. M. 2015, ApJ, 802, 18

Michałowski, M. J., Hayward, C. C., Dunlop, J. S., et al. 2014, A&A, 571, A75

Mittal, R., O'Dea, C. P., Ferland, G., et al. 2011, MNRAS, 418, 2386

Mo, H. J., Mao, S., & White, S. D. M. 1998, MNRAS, 295, 319

Narayanan, D., Hayward, C. C., Cox, T. J., et al. 2010, MNRAS, 401, 1613

Narayanan, D., Li, Y., Cox, T. J., et al. 2008, ApJS, 174, 13

Narayanan, D., Turk, M., Feldmann, R., et al. 2015, Nature, 525, 496

Neri, R., Downes, D., Cox, P., & Walter, F. 2014, A&A, 562, A35

Nikola, T., Genzel, R., Herrmann, F., et al. 1998, ApJ, 504, 749

Nyland, K., Lacy, M., Sajina, A., et al. 2017, ApJS, 230, 9

Oberst, T. E., Parshley, S. C., Stacey, G. J., et al. 2006, ApJ, 652, L125

Oliver, S. J., Bock, J., Altieri, B., et al. 2012, MNRAS, 424, 1614

Oteo, I., Ivison, R. J., Dunne, L., et al. 2016a, ApJ, 827, 34

—. 2016b, ApJ, 827, 34

Oteo, I., Zhang, Z.-Y., Yang, C., et al. 2017a, ApJ, 850, 170

Oteo, I., Ivison, R. J., Negrello, M., et al. 2017b, ArXiv e-prints, arXiv:1709.04191

Oteo, I., Ivison, R. J., Dunne, L., et al. 2018, ApJ, 856, 72

Pavesi, R., Riechers, D. A., Capak, P. L., et al. 2016, ApJ, 832, 151

Pavesi, R., Riechers, D. A., Sharon, C. E., et al. 2018, ArXiv e-prints, arXiv:1803.08048

Peng, C. Y., Ho, L. C., Impey, C. D., & Rix, H.-W. 2002, AJ, 124, 266

Pérez-González, P. G., Rieke, G. H., Villar, V., et al. 2008, ApJ, 675, 234

Pettini, M., & Pagel, B. E. J. 2004, MNRAS, 348, L59

Pierre, M., Valtchanov, I., Altieri, B., et al. 2004, J. Cosmology Astropart. Phys., 9, 011

Pineda, J. L., Langer, W. D., Velusamy, T., & Goldsmith, P. F. 2013, A&A, 554, A103

Pound, M. W., & Wolfire, M. G. 2008, in Astronomical Society of the Pacific Conference Series, Vol. 394, Astronomical Data Analysis Software and Systems XVII, ed. R. W. Argyle, P. S. Bunclark, & J. R. Lewis, 654

Rangwala, N., Maloney, P. R., Glenn, J., et al. 2011, ApJ, 743, 94

Rhoads, J. E., Malhotra, S., Allam, S., et al. 2014, ApJ, 787, 8

Riechers, D. A. 2011, ApJ, 730, 108

Riechers, D. A., Hodge, J., Walter, F., Carilli, C. L., & Bertoldi, F. 2011a, ApJ, 739, L31

Riechers, D. A., Capak, P. L., Carilli, C. L., et al. 2010, ApJ, 720, L131

Riechers, D. A., Carilli, C. L., Maddalena, R. J., et al. 2011b, ApJ, 739, L32

Riechers, D. A., Cooray, A., Omont, A., et al. 2011c, ApJ, 733, L12

Riechers, D. A., Bradford, C. M., Clements, D. L., et al. 2013, Nature, 496, 329

Riechers, D. A., Carilli, C. L., Capak, P. L., et al. 2014a, ApJ, 796, 84

Riechers, D. A., Pope, A., Daddi, E., et al. 2014b, ApJ, 786, 31

Riechers, D. A., Leung, T. K. D., Ivison, R. J., et al. 2017, ArXiv e-prints, arXiv:1705.09660

Robertson, B., Bullock, J. S., Cox, T. J., et al. 2006, ApJ, 645, 986

Robertson, B., Yoshida, N., Springel, V., & Hernquist, L. 2004, ApJ, 606, 32

Robertson, B. E., & Bullock, J. S. 2008, ApJ, 685, L27

Rodighiero, G., Daddi, E., Baronchelli, I., et al. 2011, ApJ, 739, L40

Röllig, M., Abel, N. P., Bell, T., et al. 2007, A&A, 467, 187

Rujopakarn, W., Rieke, G. H., Eisenstein, D. J., & Juneau, S. 2011, ApJ, 726, 93

Rujopakarn, W., Rieke, G. H., Weiner, B. J., et al. 2013, ApJ, 767, 73

Ruszkowski, M., & Springel, V. 2009, ApJ, 696, 1094

Saintonge, A., Kauffmann, G., Kramer, C., et al. 2011, MNRAS, 415, 32

Sakamoto, K., Wang, J., Wiedner, M. C., et al. 2008, ApJ, 684, 957

Sargent, M. T., Daddi, E., Béthermin, M., et al. 2014, ApJ, 793, 19

Savage, R. S., & Oliver, S. 2007, ApJ, 661, 1339

Scannapieco, C., Tissera, P. B., White, S. D. M., & Springel, V. 2008, MNRAS, 389, 1137

Schmidt, M. 1959, ApJ, 129, 243

Schoenmakers, R. H. M., Franx, M., & de Zeeuw, P. T. 1997, MNRAS, 292, 349

Schreiber, C., Pannella, M., Leiton, R., et al. 2017, A&A, 599, A134

Schreiber, C., Pannella, M., Elbaz, D., et al. 2015, A&A, 575, A74

Scoville, N., Murchikova, L., Walter, F., et al. 2017, ApJ, 836, 66

Shapiro, K. L., Genzel, R., Förster Schreiber, N. M., et al. 2008, ApJ, 682, 231

Sharon, C. E., Baker, A. J., Harris, A. I., & Thomson, A. P. 2013, ApJ, 765, 6

Sharon, C. E., Riechers, D. A., Hodge, J., et al. 2016, ApJ, 827, 18

Smith, D. J. B., & Hayward, C. C. 2015, MNRAS, 453, 1597

Smith, J. D. T., Croxall, K., Draine, B., et al. 2017, ApJ, 834, 5

Sofue, Y. 2017, PASJ, 69, R1

Sofue, Y., & Rubin, V. 2001, ARA&A, 39, 137

Solomon, P. M., Downes, D., Radford, S. J. E., & Barrett, J. W. 1997, ApJ, 478, 144

Solomon, P. M., & Vanden Bout, P. A. 2005, ARA&A, 43, 677

Sommer-Larsen, J., & Dolgov, A. 2001, ApJ, 551, 608

Speagle, J. S., Steinhardt, C. L., Capak, P. L., & Silverman, J. D. 2014, ApJS, 214, 15

Springel, V., & Hernquist, L. 2005, ApJ, 622, L9

Stacey, G. J., Hailey-Dunsheath, S., Ferkinhoff, C., et al. 2010, ApJ, 724, 957

Steidel, C. C., Giavalisco, M., Pettini, M., Dickinson, M., & Adelberger, K. L. 1996, ApJ, 462, L17

Steidel, C. C., Shapley, A. E., Pettini, M., et al. 2004, ApJ, 604, 534

Steidel, C. C., Rudie, G. C., Strom, A. L., et al. 2014, ApJ, 795, 165

Steinmetz, M., & Navarro, J. F. 1999, ApJ, 513, 555

Stern, D., Eisenhardt, P., Gorjian, V., et al. 2005, ApJ, 631, 163

Stevens, J. A., Amure, M., & Gear, W. K. 2005, MNRAS, 357, 361

Swaters, R. A., Sancisi, R., van Albada, T. S., & van der Hulst, J. M. 2009, A&A, 493, 871

Swinbank, A. M., Papadopoulos, P. P., Cox, P., et al. 2011, ApJ, 742, 11

Tacconi, L. J., Neri, R., Chapman, S. C., et al. 2006, ApJ, 640, 228

Tacconi, L. J., Genzel, R., Smail, I., et al. 2008, ApJ, 680, 246

Tacconi, L. J., Genzel, R., Neri, R., et al. 2010, Nature, 463, 781

Tacconi, L. J., Neri, R., Genzel, R., et al. 2013, ApJ, 768, 74

Tielens, A. G. G. M., & Hollenbach, D. 1985, ApJ, 291, 722

Tiley, A. L., Swinbank, A. M., Harrison, C. M., et al. 2018, arXiv e-prints, arXiv:1811.05982

Tully, R. B., & Fisher, J. R. 1977, A&A, 54, 661

Ueda, J., Iono, D., Yun, M. S., et al. 2014, ApJS, 214, 1

van Eymeren, J., Trachternach, C., Koribalski, B. S., & Dettmar, R.-J. 2009, A&A, 505, 1

Vitvitska, M., Klypin, A. A., Kravtsov, A. V., et al. 2002, ApJ, 581, 799

Vollmer, B., Nehlig, F., & Ibata, R. 2016, A&A, 586, A98

Walter, F., Decarli, R., Carilli, C., et al. 2012, Nature, 486, 233

Wang, R., Wagg, J., Carilli, C. L., et al. 2013, ApJ, 773, 44

Wardlow, J. L., Cooray, A., De Bernardis, F., et al. 2013, ApJ, 762, 59

Wardlow, J. L., Cooray, A., Osage, W., et al. 2017, ApJ, 837, 12

Wilson, C. D., Petitpas, G. R., Iono, D., et al. 2008, ApJS, 178, 189

Wilson, C. D., Warren, B. E., Israel, F. P., et al. 2009, ApJ, 693, 1736

Wolfire, M. G., Hollenbach, D., & McKee, C. F. 2010, ApJ, 716, 1191

Wolfire, M. G., Tielens, A. G. G. M., & Hollenbach, D. 1990, ApJ, 358, 116

Young, L. M., Scott, N., Serra, P., et al. 2014, MNRAS, 444, 3408

Younger, J. D., Fazio, G. G., Ashby, M. L. N., et al. 2010, MNRAS, 407, 1268

Zavala, J., Okamoto, T., & Frenk, C. S. 2008, MNRAS, 387, 364

Zhang, Z.-Y., Romano, D., Ivison, R. J., Papadopoulos, P. P., & Matteucci, F. 2018a, Nature, 558, 260

Zhang, Z.-Y., Ivison, R. J., George, R. D., et al. 2018b, MNRAS, 481, 59

APPENDIX

A. CO AND [CII] CHANNEL MAPS

Since we are investigating the gas kinematics, it is essential to show and acknowledge the limited significance of the detected signal *per velocity bin*. We show the channel maps for the CO ($J = 1 \to 0$) and [CII] lines in Figures 16 and 17. In the [CII] maps, structures on the scale of the angular resolution ($\lesssim 1.2$ kpc) are seen, but at low S/N significance. We therefore do not discuss the properties of potential star-forming "clumps"/structures in this paper. Exploring such direction with higher resolution and better sensitivity data would be useful to better understand the physics behind the high SFR of HXMM05.

As noted in §4.2.1, a drop off is seen in the rotation velocity beyond a radius of $R = 6$ kpc (in Figure 11). This is most likely a result of the limited S/N in the reddest velocity channels, as illustrated in Figure 16.

B. NON-DETECTION OF X-MAIN AT UV/OPTICAL WAVEBANDS

As shown in the RGB image created from *Spitzer*/IRAC 4.5 (blue), 5.8 (green), and 8 μm (red) data (Figure 8), emission detected at 4.5 μm is dominated by foreground sources (see also Figure 19), but emission at 5.8 and 8 μm is dominated by HXMM05. We therefore model the surface brightness profiles of the sources near HXMM05 based on their morphologies seen in the CFHT and VISTA images in order to de-blend the emission observed at 3.6 and 4.5 μm (see Appendix §C).

On the other hand, X-NE is detected in the UV, optical, and NIR wavebands (as shown in Figures 8 and 18). As discussed in §3, this component is also detected in CO ($J = 1 \to 0$) and [CII] line emission (see Figures 3 and 4). With the available data, we cannot discriminate and obtain reliable constraints on the stellar masses and SFRs for X-NE and X-Main separately. We thus infer the properties of the system as a whole in §5 and subsequent sections. That said, optically-selected high-z sources (e.g, BzKs, LBGs) appear to be different populations from these highly dusty starburst galaxies (possibly due to different evolutionary stages), and surveys done at only one wavelength are likely to miss other high-z candidates in the field. Given that X-NE is optically visible, and thus may have less dust than X-Main, it may be a young nearby galaxy soon to be engulfed by X-Main. We report the pair's gas mass ratios in Table 7. More observations will be useful to better understand the physical properties of X-NE, and thus, its nature in relation to X-Main in the HXMM05 system.

C. DE-BLENDING *SPITZER*/IRAC EMISSION

Multiple sources are detected near HXMM05 at 3.6 and 4.5 μm (channels 1 and 2; Figures 18 and 19). We examine whether part of the emission detected at 3.6 and 4.5 μm may arise from HXMM05 by using the publicly available software GALFIT (Peng et al. 2002) to de-blend the emission. We initialize the fitting parameters based on the positions, brightnesses, and morphologies of the sources near HXMM05 as observed in the higher resolution NIR images (*HST*/WFC3 F110W, VISTA, and CFHT; see e.g., Figure 18). We use a total of six components and a sky background to account for all the emission detected in the high resolution NIR images. We model the surface brightness distributions of the two brightest components using Sersic profiles, each with seven free parameters: x, y, I, R_e, n, b/a, and PA, where x and y describe the position of the component, I is the integrated flux, R_e is the effective radius, n is the Sersic index, b/a is the axial ratio, and PA is the position angle. We model the remaining four components as point sources, for which we adopt the point response functions (PRF), described by three free parameters x, y, and I per source. We allow all parameters to vary without imposing any priors in order to avoid biasing the best-fit parameters. The PRFs are adopted from the IRAC calibration routines[40]. We do not detect any statistically significant emission at the position of HXMM05 in the residual maps (Figure 19). We thus adopt the SWIRE survey depths at the two IRAC wavebands as 3σ upper limits (Table 2).
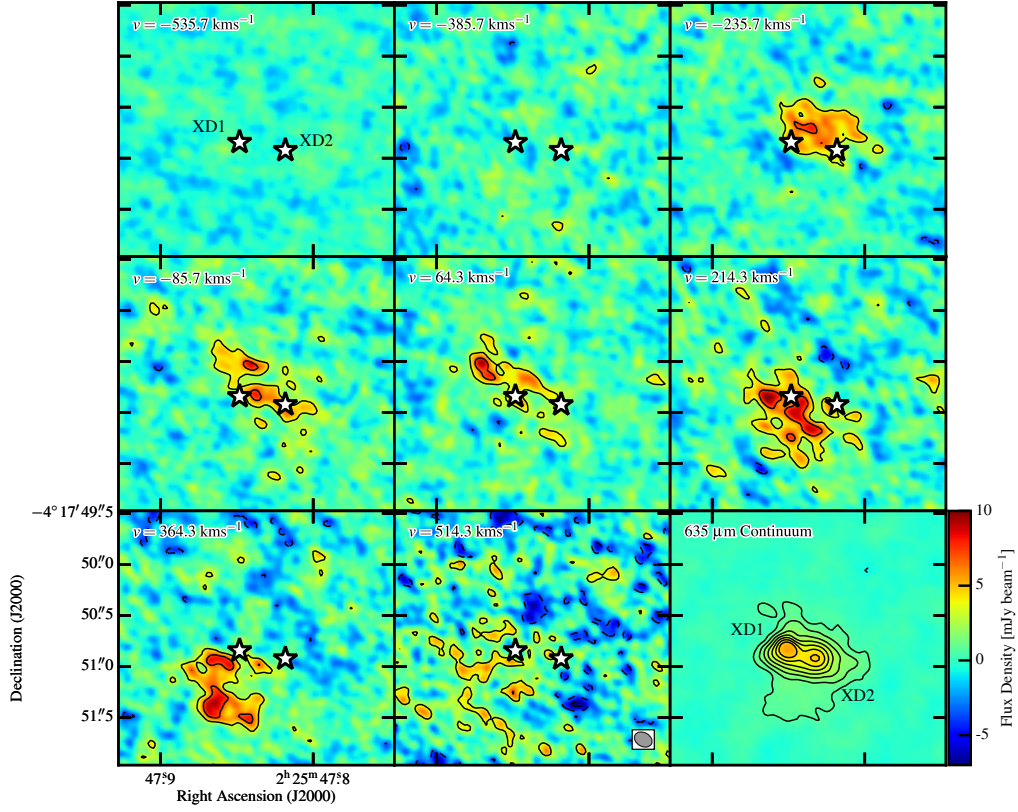
---

[40] http://irsa.ipac.caltech.edu/data/SPITZER/docs/irac/calibrationfiles/psfprf/

Figure 16. Channel maps of the [CII] line emission in X-Main shown at full spatial resolution with velocity bins of $\Delta v = 150\,\mathrm{km\,s^{-1}}$. Last panel shows the 635 μm continuum underlying the [CII] line. The central velocity of each panel is indicated at the upper left corner. Contours are shown in steps of $[-3, 3, 6, 9] \times \sigma_{\mathrm{ch}}$, where $\sigma_{\mathrm{ch}} = 1.15\,\mathrm{mJy\,beam^{-1}}$ (0.22 mJy beam^{-1} for the continuum). The last channel (i.e., second last panel) is dominated by noise since it is near the edge of a spectral window, where an atmospheric feature is present. Black markers indicate the positions of the 635 μm dust peaks (XD1 and XD2; see last panel). Synthesized beam size is shown in the lower right corner of the second last panel (same as the leftmost panel in Figure 4). X-NE is outside the field-of-view shown here.
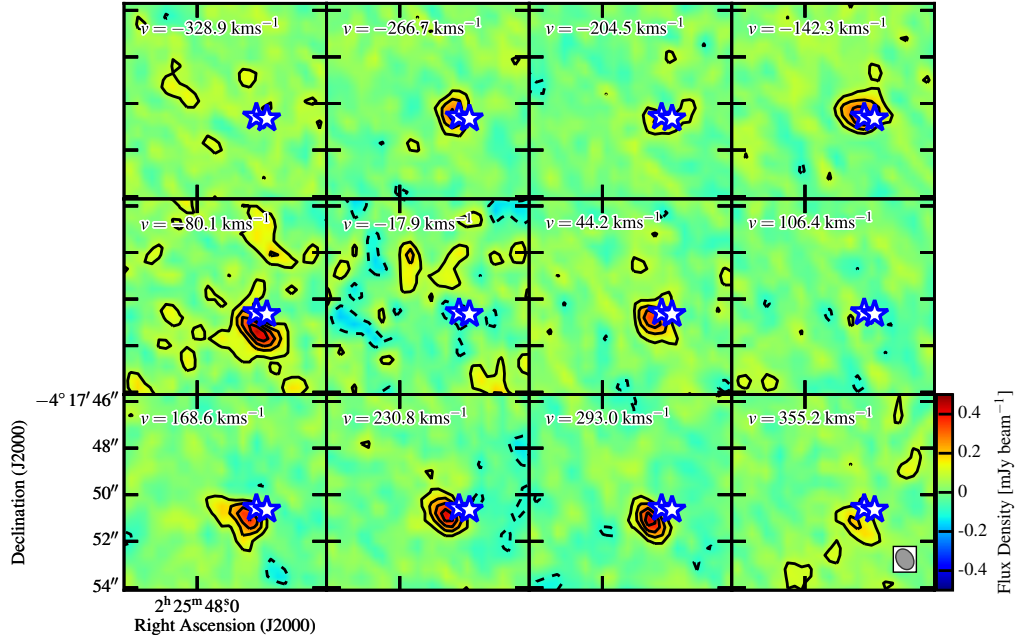

Figure 17. Channel maps of CO $(J = 1 \rightarrow 0)$ emission imaged with Briggs weighting, covering a velocity range of $\Delta v \in [-626, 712]\,\mathrm{km\,s^{-1}}$. Number in the upper left corner of each panel indicates the central velocity v_{LSR} of each map, where the emission is integrated over $\Delta v = 145\,\mathrm{km\,s^{-1}}$. The CO $(J = 1 \rightarrow 0)$ emission is marginally spatially resolved. The emission centroid shifts from NW to SE with increasing velocity. Contours are shown in steps of $[-3, 3, 4, 5, 6, 9] \times \sigma_{\mathrm{ch}}$, where $\sigma_{\mathrm{ch}} = 0.031\,\mathrm{mJy\,beam^{-1}}$. The star symbols indicate the positions of the two compact dust components detected at 635 μm (rest-frame 158 μm; XD1 and XD2; see last panel of Figure 16). The synthesized beam is shown in the lower right corner of the last panel ($0''.94 \times 0''.71$ at PA $= 31°$).

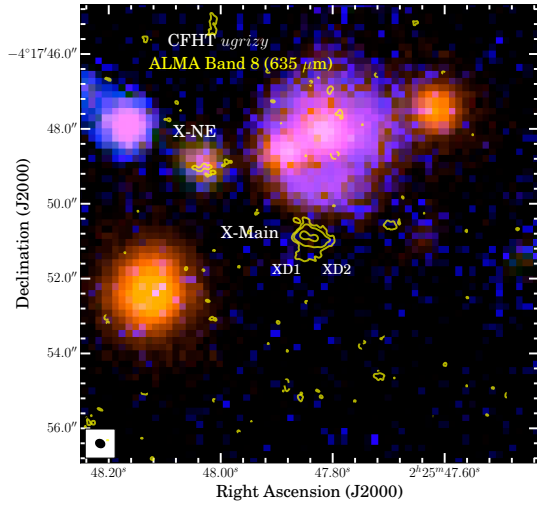**Figure 18.** ALMA 635 μm continuum emission (yellow contours) overlaid on UV/optical/IR images: u^*- (blue), $g'r'i'$- (green), and z'-bands (red) obtained with the CFHT at $0\rlap{.}''8$ resolution. Contours are shown in steps of $[-3, 3, 6, 18] \times \sigma_{635}$, where $\sigma_{635} = 0.22$ mJy beam^{-1}. The synthesized beam for the ALMA data is shown in the lower left corner. The main component of HXMM05 (X-Main) remains undetected, whereas X-NE is detected in the UV/optical/NIR wavebands and in the CO ($J = 1 \rightarrow 0$) and [CII] lines (see Figures 3 and 4).
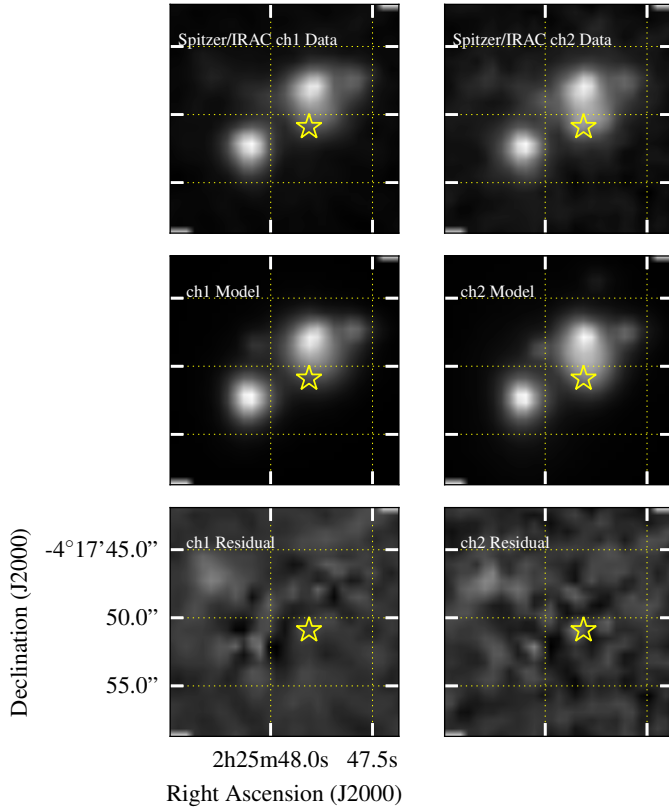

Figure 19. Top: *Spitzer*/IRAC images at 3.6 (ch1) and 4.5 μm (ch2). Middle: GALFIT models. Bottom: Residual maps, showing that HXMM05 remains undetected after de-blending. Yellow symbols indicate the position of the HXMM05 system.